

2008-01-01

Study of Structural and Spectroscopic Properties of Small ZnS Clusters by DFT

Venkata Ramana Chaganti

University of Texas at El Paso, vrchaganti@miners.utep.edu

Follow this and additional works at: https://digitalcommons.utep.edu/open_etd



Part of the [Condensed Matter Physics Commons](#)

Recommended Citation

Chaganti, Venkata Ramana, "Study of Structural and Spectroscopic Properties of Small ZnS Clusters by DFT" (2008). *Open Access Theses & Dissertations*. 226.

https://digitalcommons.utep.edu/open_etd/226

This is brought to you for free and open access by DigitalCommons@UTEP. It has been accepted for inclusion in Open Access Theses & Dissertations by an authorized administrator of DigitalCommons@UTEP. For more information, please contact lweber@utep.edu.

STUDY OF THE STRUCTURAL AND SPECTROSCOPIC
PROPERTIES OF SMALL ZnS CLUSTERS BY DFT

VENKATA R CHAGANTI

Department of Physics

APPROVED:

Tunna Baruah, Ph.D., Chair

Murat Durandurdu, Ph.D.

Russell R. Chianelli, Ph.D.

Rajendra R. Zope, Ph.D.

Patricia D. Witherspoon, Ph.D.
Dean of the Graduate School

TO MY MOTHER AND SISTERS

STUDY OF THE STRUCTURAL AND SPECTROSCOPIC
PROPERTIES OF SMALL ZnS CLUSTERS BY DFT

By

VENKATA R CHAGANTI, B.E.

THESIS

Presented to the Faculty of the Graduate School of

The University of Texas at El Paso

in Partial Fulfillment

of the Requirements

for the Degree of

MASTER OF SCIENCE

Department of Physics

THE UNIVERSITY OF TEXAS AT EL PASO

DECEMBER 2008

ACKNOWLEDGMENTS

I would like to express my deep gratitude to the College of Science, UTEP for supporting me as a Research Assistant which made this work possible. I want to thank our Chair Dr. Jorge Lopez for giving me the opportunity to join as a graduate student at UTEP. I would like to thank all the faculty of Physics Department, UTEP in providing valuable lectures which directly or indirectly helped me in my progress towards completing my thesis. I would also like to express my gratitude to the department office staff and the office supervisor Terry Weber who has helped me in a number of occasions. I thank Dr. Tunna Baruah who has been my supervisor for this thesis. I want to thank Dr. Rajendra R. Zope, whose tireless help and devotion of time for guiding me to become a computational student and imparting the knowledge into the work made this thesis a completion. I am deeply indebted to my mother and sisters who have been constantly encouraging and supporting me financially to do my graduation. I would like to specially thank the developers of NRLMOL whose package is used for computational purpose.

Presented to the thesis committee

December 3, 2008

ABSTRACT

The small clusters (aggregates of atoms containing a few tens of atoms) of semiconductors and metals often adopt very different shapes than the fragments of these materials in the bulk phase. Due to their large surface to volume ratio and unsaturated bonds, the small clusters often have properties that are very different from their bulk. Semiconductor clusters are extensively studied for their potential applications in a wide variety of systems from opto-electronic devices to spintronics. The present work is devoted to understanding the structural and electronic properties of small clusters of the zinc sulfide Zn_nS_n where $n = 1 - 6$. The equilibrium structures of the clusters are obtained by starting with several possible atomic configurations and optimizing these geometries. The calculations are performed using density functional theory. The calculations are carried out using advanced electronic structure package called NRLMOL. The calculations are free from pseudo potential approximation i.e. both valence as well as core electrons are explicitly treated in calculations. The nature of each local minimum (structure) is analyzed by computing the vibrational frequencies within the harmonic approximation. The electronic properties such as ionization energies, the band gap (HOMO-LUMO gap), and electron affinity are obtained for all the stable structures. Additionally, spectroscopic properties such as infrared and Raman spectra are obtained which will be helpful in possible detection and identification of these clusters in experiment. The evolutions of all these properties are studied as a function of the size of clusters.

TABLE OF CONTENTS

	Page
ACKNOWLEDGMENTS.....	iv
ABSTRACT.....	v
TABLE OF CONTENTS	vi
Chapter	
1. INTRODUCTION	1
1.1 ZnS	5
1.2 Band gaps or HOMO-LUMO gaps in semiconductors	6
1.3 Photovoltaic cells	11
1.4 Photo Catalyst	12
2. METHOD.....	14
2.1 Density Functional Theory	14
2.2 Basis Set Method	19
2.3 Computational Details	21
2.4 General Rules Concerning Vibrations	22
2.5 IR Spectroscopy	24
2.6 Raman Spectroscopy.....	27
3. RESULTS AND DISCUSSIONS.....	32
3.0 Geometrical Structures of Neutral and Singly Charged (Positive & Negative) ZnS Clusters	32
3.1 ZnS	32

3.2 Zn ₂ S ₂	34
3.3 Zn ₃ S ₃	36
3.4 Zn ₄ S ₄	37
3.5 Zn ₅ S ₅	40
3.6 Zn ₆ S ₆	41
3.7 Data on Structural and Electronic Properties	42
3.8 HOMO-LUMO Gaps	44
3.9 IR and Raman Spectra	47
3.10 Dipole Moment and Polarizability	59
SUMMARY	62
APPENDIX	64
Definitions	64
REFERENCES	65
CURRICULUM VITAE.....	70

Chapter 1

INTRODUCTION

The development of the electronics has led to decrease of component sizes. The aim of this trend is not only to increase the integration level, but mainly, to increase the operation speed. Moreover, several specific phenomena can be observed only when the elements have very small sizes. In recent years the study of atomic clusters has become an increasingly active research field for their unique properties which are different from their extended bulk states or from atomic states. The clusters have large surface to volume ratio which plays a crucial role in determining their unique properties. Thus the study of the size evolution of their properties, such as their optical, electrical, chemical, magnetic, catalytic properties which can be exploited for developing new technology has gained tremendous importance. It is found that cluster properties change from molecular to bulk properties as a function of size. In spite of the fact that very large enough clusters have bulk like properties, small clusters have become interesting as the cluster and nano-particle characterization is technologically possible.

Photovoltaic cells, quantum devices, photo catalysts are playing an important role in the development of electronic industrial world. All these devices use special type of semiconductors. Therefore it has led to extensive search for special semiconductors. Materials suitable for quantum devices, photovoltaic cells [1-4], photo catalysts [5] or optical sensitizers [6] have been increasing. Materials suitable for these devices are undoubtedly semiconductors. Group II – VI compound semiconductors are found to be suitable for the applications in the above devices. The band gaps of these compounds make them especially interesting for photovoltaic cells. Within the visible region the

electromagnetic spectrum extends from 1.8 eV to 3.1 eV. Therefore, a good material for its use in photovoltaic solar cells must have band gaps close to the given energies. Another field where dilute magnetic semiconductor materials are being investigated is “spintronics” where apart from charge the spin of the carrier is also important [7].

Since these semi-conductors (II–VI) are versatile materials, extensive experimental and theoretical studies are made to improve practical devices. Computational studies can predict the properties of clusters quite accurately at the small size regime of a few hundreds of atoms at the density functional theory (DFT) level. Small clusters of II-VI semiconductors such as CdO, ZnO, ZnSe, ZnTe, CdS, and CdSe have been extensively studied at the level of DFT [8-12]. However, there are a small number of studies performed on the small ZnS clusters. In this project, we have carried out density functional calculations on very small stoichiometric Zn_nS_n clusters up to the size $n=6$. There are a large number of experimental studies on the photo-physical properties of ZnS quantum dots [13]. These studies are mostly done on capped ZnS quantum dots and the particle sizes are quite large compared to the clusters studied here. At the smaller size regime, there are a number of experimental studies done on the mass spectrum and mainly on the optical properties of ZnS clusters both stoichiometric and non-stoichiometric. It was found that non-stoichiometric clusters are more abundant than stoichiometric clusters. There are also a few computational studies reported for ZnS molecular clusters and crystallites of up to several hundred atoms. Theoretical studies of ZnS have been reported in [14-15]. A number of studies have been done the ZnS “bubbles” or cages and also on the nanotubes [16-17]. Some of the excellent works are

those of Muillu and Pekkanen [18], Pollmann and co-workers [19–20], Krum Chuchev and group [21], Pal and his coworkers [22], Spano et al. [17], L.Brus [23].

The early works of Brus et al. were mostly studies on the quantum confinement effects ZnS quantum dots using an empirical spherical well potential [23]. Muillu and Pekkanen performed a Hartree-Fock study on the surfaces of ZnS nanocrystallites. Since it is a Hartree-Fock calculation, they have not considered the electron correlation. Restricted Hartree-Fock method was applied to small ZnS clusters up to eight total atoms in [24]. Only structure that was converged was the stoichiometric tetramer. In their calculations the structures of the clusters were assumed as cut-outs of bulk ZnS. Density functional theory with pseudo-potentials was used by Ugalde group [10] for Zn_nS_n for sizes $n \leq 9$. They found that for clusters up to size $n=5$, the structures adopted planar and monocyclic rings. For $n \geq 6$, three-dimensional structures became more stable. Ugalde and group [8-9] also studied the low lying excited states of the $(ZnS)_n$ clusters and estimated the electronic excitation energies using both configuration interaction singles (CIS) and time-dependent density functional theory (TDDFT).

The current study is carried out to explore geometrical, electronic and spectroscopic properties of small clusters of ZnS and to learn about computational electronic structure methods. The goal is to study structural, electronic and spectroscopic properties of Zn_iS_i , where $i = 1 - 6$, using advanced electronic structure calculation package NRLMOL. There may be several structures possible for each 'i' in Zn_iS_i . Structures could be of planar ring type or three-dimensional. Geometries up to size $n=6$ were optimized and all the possible optimized structures are further tested for vibrational stability. For each size, the bond lengths and bond angles are compared with earlier

reported works. Vertical and adiabatic ionization energies, vertical and adiabatic electron affinities, the energy gaps between the highest occupied molecular orbital and the lowest unoccupied molecular orbitals (HOMO-LUMO gaps) were calculated for the lowest energy structures. Based on the theoretical values of gaps, probable applications for these materials are predicted and suggested. In addition, the dipole moments and mean Polarizabilities were calculated. Finally infrared and Raman Spectra for the lowest energy structures were obtained for possible detection and identification of these small clusters in experiments.

Semiconductor materials

In this section we describe the ZnS bulk properties, some of the relevant concepts of band theory, general properties of semiconductor materials, and their applications as photo-voltaics and photo-catalysts.

1.1 ZnS

Cubic Zinc Sulfide Structure

The diamond structure of bulk ZnS may be viewed as two FCC structures displaced from each other by one-quarter of a body diagonal. The cubic zinc sulfide (zinc blende) structure results when Zn atoms are placed on one FCC lattice and S atoms on the other FCC lattice, as in Figure 1.1.

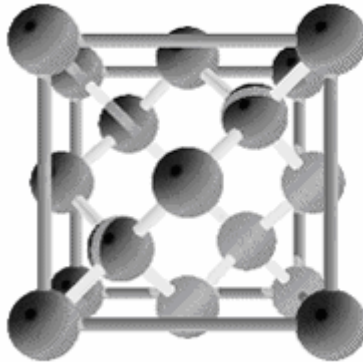


Fig. 1.1: The zinc blende structure

The conventional cell is cube. The coordinates of the Zn atoms are 000 ; $0\frac{1}{2}\frac{1}{2}$; $\frac{1}{2}0\frac{1}{2}$; $\frac{1}{2}\frac{1}{2}0$; the coordinates of the S atoms are $\frac{1}{4}\frac{1}{4}\frac{1}{4}$; $\frac{1}{4}\frac{3}{4}\frac{3}{4}$; $\frac{3}{4}\frac{1}{4}\frac{3}{4}$; $\frac{3}{4}\frac{3}{4}\frac{1}{4}$. The lattice is FCC. There are four molecules of ZnS per conventional cell. Around each atom there are four equally distant atoms of the opposite kind arranged at the corners of a regular tetrahedron.

In crystals, the diamond arrangement is shown by C, Si, Ge, and Sn, and the sphalerite or the wurtzite arrangement (or both) by the compounds SiC, AlN, AlP, AlAs, AlSb, GaP, GaAs, GaSb, InSb, ZnO, ZnS, ZnSe, ZnTe, CdS, CdSe, CdTe, HgS, HgSe, HgTe, CuCl, CuBr, CuI, AgI, MgTe, BeO, BeS, BeSe, and BeTe. In all of these except BeO it is probable that the bonds are essentially covalent in structure with some ionic character [25].

In ZnS the extreme covalent structure places formal charges 2^- on zinc and 2^+ on sulfur. It is probable that the bonds have enough ionic character in this crystal and in others of similar structure to make the actual charges of the atoms nearly zero; for ZnS this would require about 50 percent ionic character. The ZnS bond length is approximately 2.35 Angstrom [25]. The fractional ionic character of bonds in ZnS as given by [26] is about 0.62. The band gap in ZnS is about 3.91eV for wurtzite and 3.84eV for zinc blende [27].

1.2 Band gaps or HOMO-LUMO gaps in semiconductors

HOMO stands for highest occupied molecular orbital and LUMO stands for lowest unoccupied molecular orbital respectively. The difference of the energies of the HOMO and LUMO gives the measure of the excitability of the molecule and is termed as band gap. When considering electronic properties and certain optical properties, a band theory description is necessary.

When the molecule forms an aggregate, the proximity of the orbitals of the different molecules induce a splitting of the HOMO and LUMO energy levels. This

splitting produces sublevels which each have their own energy, slightly different from one another. When there are enough molecules influencing each other, there are so many sublevels that we no longer perceive their discrete nature and they form a continuum. We no longer consider energy levels, but energy bands.

Band theory describes a non-metallic material as having essentially two energy bands. The lower energy valence band (completely filled) and the upper energy conduction band (completely empty) at 0 K. The energy separating the top of the valence band and the bottom of the conduction band is called band gap E_g and is expressed in eV (electron volt = 1.602×10^{-19} J). For a compound M_aA_z , the oxidation number concept allows us to regard the valence band as filled with electrons 'belonging' to A^a , while the conduction band is composed of empty orbitals 'belonging' to M^{z+} . Since ZnS is 0.62 fractional ionic, this description should be adequate.

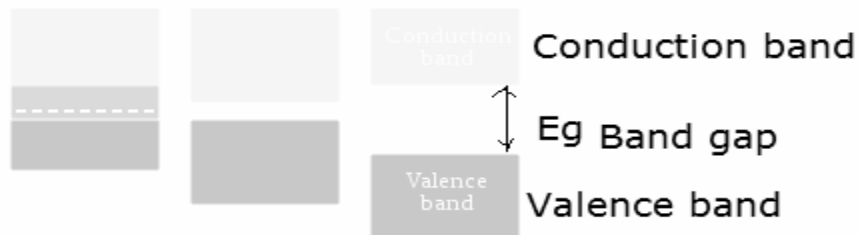


Fig. 1.2: The energy bands in a bulk semiconductor

Energies greater than or equal to E_g (provided they do not exceed the difference between the bottom of the valence band and top of the conduction band) will promote

electrons from valence band to the conduction band. Thus, the optical absorption arising from such transitions gives rise to very broad absorption bands. In simple cases where symmetry allows, the onset of the intense optical absorption occurs at the photon energy corresponding to the band gap, and this provides a method for estimating E_g experimentally.

The valence band and conduction band each represent a range of energy, E , which varies with the wavelength, λ , of the waves which, in terms of the tight binding approach, result from combinations of the various atomic orbitals of M^{Z+} and A^{a-} . For example for GaAs, the maximum in E for the valence band and the minimum in E for the conduction band occur at the same value of k (quantum number), and therefore the minimum energy (E_g) for the transition from valence band to the conduction band involves no change in k . This is direct transition. The materials that have different values of k for maximum of valence and minimum of conduction have indirect electronic transition.

Electronic transitions involving no change of k have a higher probability than those where k is required to change and therefore have greater oscillator strengths. The accompanying wavelength change for an indirect transition requires coupling of the crystal vibrations (phonons) to make the electronic transition allowed. The indirect transitions are described as phonon assisted. The onset of optical absorption for an indirect gap material often occurs more gradually than for a direct gap material.

The visible region of the spectrum is for photon energies between 1.8 eV and 3.1 eV. Since the onset of optical absorption corresponds to the magnitude of the band gap,

E_g , it is anticipated that materials with large band gaps (over 3.1 eV) will be white or colorless. Alternatively, any color will be due to some electronic transition not involving the band gap. A list of some important materials with their band gaps is in Table 1.1 [27]. The transfer of electrons from valence band to conduction band can be achieved by optical absorption as well as by thermal excitation. At ordinary temperatures, particularly in systems with small gaps, due to thermal excitations some electrons from the valence band jump into the conduction band. The lower the value of E_g , the greater the extent of thermal population of the conduction band, and materials for which this effect is significant are called semiconductors. The thermal population of conduction band increases with increase in temperature.

If a semiconductor is exposed to light and the photon energy is gradually increased, there will be a large increase in conductivity at the point when the photon energy equals E_g . Materials responding very well to this effect are called photoconductive materials. The electrical resistance of these materials drops according to the light intensity once the photon energy reaches the value of E_g .

Materials with E_g greater than 4 or 5 eV are described as insulators. In terms of tight binding approach, powerful covalent bonding results in a large energy difference between bonding and antibonding states, and hence to a large band gap. In the case of electrovalent compounds, overcoming the band gap involves transferring an electron essentially from the anion to the cation, and the energy required for this increases with increasing electrovalency. Conversely, a good semiconductor (of low E_g) results when there is low ionic character and the covalency is weak.

Electron transfer process in a simple compound, such as CdS or ZnS, is similar to that in a complex ion such as $[\text{PbCl}_6]^{2-}$. Essentially, in simple compounds the electronic transitions are between energy bands whereas for complex ions they are between discrete energy levels (molecular orbits). The band gap, E_g (in eV) is given by:

$$E_g = 3.72 [X^*(\text{anion}) - X^*(\text{cation})] \quad (1.1)$$

Where X^* is the optical electronegativity of the cation or anion. Table 1.2 [27] gives the optical electronegativities of the II-VI semiconductors.

Table 1.1 Important materials with their band gaps.

Type	Formula	Structure or coordination	E_g eV	Type	Formula	Structure or coordination	E_g eV
Elements	C	Diamond	5.4	Elements	Si	Diamond	1.11
Elements	Ge	Diamond	0.67	Elements	$\text{Sn}(\alpha)$	Diamond	0.08
Elements	As	Layer structure	1.2	Elements	Sb	Layer structure	0.1
Elements	Se	Hexagonal	1.6	Elements	Te	Hexagonal	0.4
III-V	AlP	Zinc blende	3.0	III-V	AlAs	Zinc blende	2.3
III-V	AlSb	Zinc blende	1.52	III-V	GaN	Zinc blende	3.34
III-V	GaP	Zinc blende	2.24	III-V	GaAs	Zinc blende	1.43
III-V	GaSb	Zinc blende	0.70	III-V	InP	Zinc blende	1.27
III-V	InAs	Zinc blende	0.36	III-V	InSb	Zinc blende	0.17
IIB-VI	ZnO	Wurtzite	3.4	IIB-VI	ZnS	Wurtzite	3.91
IIB-VI	ZnS	Zinc blende	3.84	IIB-VI	ZnSe	Zinc blende	2.83
IIB-VI	ZnTe	Zinc blende	2.39	IIB-VI	CdO	Rocksalt	2.5
IIB-VI	CdS	Wurtzite	2.58	IIB-VI	CdSe	Wurtzite	1.84

Table 1.2 Optical electronegativity of group II & IV semiconductors

II	Optical electronegativity	VI	Optical electronegativity
Zn^{2+}	1.1	S^{2-}	2.15
Cd^{2+}	1.45	Se^{2-}	1.9
Hg^{2+}	1.55	Te^{2-}	1.8

1.3 Photovoltaic cells [28]

Photovoltaic cells, more commonly known as solar cells, are found in devices such as calculators and satellites. First used almost exclusively in space, photovoltaic cells are used in more common applications. In simple terms, photovoltaic cells and devices convert light energy into electrical energy. Photovoltaic cells are available in many different shapes and sizes. When individual photovoltaic cells are joined, they form photovoltaic modules.

Semiconductors are used for the construction of photovoltaic cells. The most commonly used semiconductor material for the construction of photovoltaic cells is silicon. Several forms of silicon are used for the photovoltaics: they can be single-crystalline, multi-crystalline, and amorphous. The molecular structure of single-crystal silicon is uniform. This uniformity is ideal for the transfer of electrons efficiently through the material. However, in order to make an effective photovoltaic cell, silicon needs to be "doped" with other elements. Although multi-crystalline silicon is normally considered less efficient than single-crystal silicon, they are less expensive to produce. Amorphous silicon can absorb 40 times more solar radiation than single-crystal silicon. This is one of the main reasons why amorphous silicon can reduce the cost of photo-voltaics. Amorphous silicon can be coated on low-cost substrates such as plastics and glass. Numerous thin-film technologies are currently being developed to decrease the amount of light absorbing material required to produce solar cells. This could lead to a reduction in the processing costs; however it could also lead to a reduction in the energy conversion efficiency. The thin films of copper indium diselenide, cadmium telluride, and gallium

arsenide have very high absorptivity. Sometimes the efficiency is increased by doping these materials with some impurity. It requires only a film of a few microns to absorb 99% of the incident light.

1.4 Photo Catalyst

Environmental pollution and destruction on a global scale have drawn attention to the vital need for totally new environmentally friendly, clean chemical technologies and processes, the most important challenge facing chemical scientists in the field of green chemistry. Strong contenders as environmentally harmonious catalysts are photo catalysts that operate at room temperature and in a clean manner. Applications of such safe photo catalytic systems are urgently desired for the purification of polluted water, the decomposition of offensive atmospheric odors as well as toxins, the fixation of CO₂, and the decomposition of NO_x and chlorofluorocarbons on a huge global scale. To address such enormous tasks, photo catalytic systems that are able to operate effectively and efficiently not only under UV light but also under the most environmentally ideal energy source, sunlight, must be established.

The fact that using energy to eliminate environmental contamination increases emission of CO₂ resulting in more global warming. Under such circumstances, we need new materials that can gently harmonize the contaminated environment to restore original conditions by using natural energy. One solution to that problem is photo-catalyst. Photo-catalyst produces surface oxidation to eliminate harmful substances such as organic compounds or nearby bacteria, when it is exposed to the sun or fluorescent lamp. When

titanium oxides or such materials are irradiated with UV light that is greater than the band gap energy of the catalyst ($\lambda < 380 \text{ nm}$), electrons and holes are produced in the conduction and valence bands, respectively. The electrons have a highly reactive reduction potential while the holes have a highly reactive oxidation potential, which together induce catalytic reactions on the catalyst surfaces—namely, photo catalytic reactions. Because of its similarity to the mechanism observed with the photosynthesis in plants, photo catalysis may also be referred to as artificial photosynthesis. There are no limits to the possibilities and applications of semiconductor photo catalysts and photo catalytic reactions as “environmentally harmonious catalysts”. By applying this principle to water treatment, dissolving NO_x in the air, or room air purification, photo-catalyst can be used for various steps in purifying a contaminated environment.

Chapter 2

METHOD

All calculations in the present work have been performed within the framework of density functional theory (DFT). Below we will briefly describe the basic concepts in DFT.

2.1 Density Functional Theory

The roots of modern density functional theory [29-36] can be traced back to the early days of quantum theory when Thomas and Fermi used models for the electronic structure of atoms which depend only on the electron density [37, 38]. Later the Hartree-Fock-Slater or the $X\alpha$ method was introduced to be used in studies on systems with more than one atom. From today's perspective it represents one of the first density functional methods. It emerged from the work of Slater [39] who proposed to replace the complicated, non-local exchange term of the Hartree-Fock (HF) method by the approximate local exchange potential of Dirac [40], which is simply given by $\rho^{1/3}$. However, it was not until 1964 when DFT was put on a firm basis by the celebrated theorems of Hohenberg and Kohn [41], later generalized by Levy [42], which state that all properties of an electronic system are functionals of the ground state electron density. In particular, the ground state energy of a many-electron system in an external potential, i.e., the potential due to a set of nuclei in a given arrangement, can be found by minimizing the functional of the total electronic energy with respect to variations in the density. Parr and Yang [30] have reviewed how major chemical concepts follow from the existence of such a functional.

Unfortunately, it is very difficult to develop sufficiently accurate density functionals, in particular, for the kinetic energy. This is a problem that already plagued the Thomas-Fermi approach. Although the Hohenberg-Kohn theorems give a theoretically sound basis for the Thomas-Fermi approach and DFT in general, the practical importance of DFT might not have risen above that of the Thomas-Fermi model if it had not been for the ingenious idea of Kohn and Sham [43] to model the kinetic energy of the real, interacting N-electron system by that of a system of N non-interacting electrons.

In Kohn-Sham (KS) theory [43], the total electronic energy is given as

$$E[\rho] = T_s[\rho(\vec{r})] + \int d\vec{r} \rho(\vec{r}) v_{\text{ext}}(\vec{r}) + \frac{1}{2} \int d\vec{r}_1 d\vec{r}_2 \rho(\vec{r}_1) r_{12}^{-1} \rho(\vec{r}_2) + E_{\text{xc}}[\rho(\vec{r})], \quad (2.1)$$

with $r_{12} = |\vec{r}_1 - \vec{r}_2|$. The various terms represent, in order, the kinetic energy of the KS system (the fictitious system of non-interacting electrons), the interaction between electrons and the external potential v_{ext} generated by the nuclei and external fields, the Hartree energy arising from the Coulomb interactions of the electrons, and the remainder of the total energy which is referred to as the exchange-correlation (XC) energy E_{xc} . Note that E_{xc} , which is a crucial quantity in DFT, is defined with the help of the KS system and not with respect to the HF wave function as in traditional quantum chemical methods. The electron density is obtained from the KS wave function, i.e., from a reference wave function of non-interacting electrons which is simply a Slater determinant built from the eigenfunctions ψ_i of a single-particle Hamiltonian. For a closed-shell system one obtains

$$\rho(\vec{r}) = 2 \sum_i^{occ} |\psi_i(\vec{r})|^2, \quad (2.2)$$

the sum extending over all occupied KS or molecular orbitals (MOs) ψ_i . An extension to the spin-polarized case is straightforward and shall not be considered here. The functional T_s representing the kinetic energy of the non-interacting electrons is then given as

$$T_s[\rho(\vec{r})] = 2 \sum_i^{occ} \left\langle \psi_i \left| -\frac{\nabla^2}{2} \right| \psi_i \right\rangle. \quad (2.3)$$

It must not be identified with the exact kinetic energy of the real system of interacting electrons. The important point is that it is a convenient and fairly good approximation to the exact kinetic energy based on the KS orbitals. The remainder of the exact kinetic energy is taken into account as part of the XC energy E_{xc} .

According to the second Hohenberg-Kohn theorem [41] the ground state electron density minimizes $E[\rho]$ and hence must satisfy the Euler-Lagrange equation

$$\frac{\delta E[\rho]}{\delta \rho(\vec{r})} = \frac{\delta T_s}{\delta \rho(\vec{r})} + v_{ext}(\vec{r}) + v_h(\vec{r}) + v_{xc}(\vec{r}) = \mu. \quad (2.4)$$

Here,

$$v_h(\vec{r}) = \int d\vec{r}_2 r_{12}^{-1} \rho(\vec{r}_2) \quad (2.5)$$

And
$$v_{xc}(\vec{r}) = \frac{\delta E_{xc}[\rho(\vec{r})]}{\delta \rho(\vec{r})}, \quad (2.6)$$

are the Hartree and the XC potential, respectively. The Lagrange multiplier μ takes the constraint

$$\int d\vec{r} \rho(\vec{r}) = N \quad (2.7)$$

into account, where N is the number of electrons, thus guaranteeing charge conservation. Since for T_s as explicit density functional no sufficiently accurate approximations are available, it is written as an orbital functional [Eq. (2.3)] and therefore Eq. (2.4) cannot be solved directly, i.e., one cannot directly minimize Eq. (2.1) with respect to ρ in order to obtain the ground state energy and density. Instead, this minimization is performed indirectly. For the non-interacting electrons moving in a potential $v_s(\mathbf{r})$, the corresponding Euler-Lagrange equation is

$$\frac{\delta E_s[\rho(\vec{r})]}{\delta \rho(\vec{r})} = \frac{\delta T_s[\rho(\vec{r})]}{\delta \rho(\vec{r})} + v_s(\vec{r}) = \mu. \quad (2.8)$$

The density solving this equation is ρ_s . Comparing Eq. (2.8) with Eq. (2.4) shows that both have the same solution $\rho = \rho_s$, if v_s is chosen to be

$$v_s(\vec{r}) = v_{ext}(\vec{r}) + v_h(\vec{r}) + v_{xc}(\vec{r}). \quad (2.9)$$

Consequently, the density of the interacting (many-body) system in the external potential v_{ext} can be obtained by solving the one-electron Schrodinger equations

$$\hat{H}^{KS} \psi_i(\vec{r}) = \epsilon_i \psi_i(\vec{r}) \quad (2.10)$$

with the KS single-particle Hamiltonian

$$\hat{H}^{KS} = -\frac{\nabla^2}{2} + v_{ext}(\vec{r}) + v_h(\vec{r}) + v_{xc}(\vec{r}) \quad (2.11)$$

and the canonical MO energies ϵ_i . Once the KS orbitals have been determined from Eq. (2.10), the total electronic energy of the real, interacting system can be obtained from Eq. (2.1).

Eq. (2.10) is somewhat deceptive, in that it looks like a simple single-particle Schrodinger equation. However, two features bring out the full many-body character of the problem. One is that Eq. (2.10) has to be solved self-consistently since both v_h and v_{xc} depend on the electron density ρ which is a function of the KS orbitals ψ_i . The other is the incomplete knowledge of the XC energy density functional E_{xc} .

Exchange-correlation functionals

The KSDFT expression for the total energy is exact. However, practical implementation requires use of approximation for the exchange-correlation functional. The success of the KS method hinges on the availability of good approximations to E_{xc} .

For many years the most widely used scheme has been the so-called local density approximation (LDA),

$$E_{xc}^{LDA}[\rho(\vec{r})] = \int d\vec{r} \epsilon_{xc}(\vec{r}) \rho(\vec{r}), \quad (2.12)$$

where ϵ_{xc} is the XC energy density in a homogeneous electron gas, known with great accuracy from quantum Monte-Carlo calculations [44]. This approximation is obviously valid in the limit of slowly varying densities, but has proven its accuracy for a wide range of systems. The function E_{xc}^{LDA} can be divided into exchange and correlation contributions,

$$E_{xc}^{LDA}[\rho] = E_x^{LDA}[\rho] + E_c^{LDA}[\rho], \quad (2.13)$$

where the exchange contribution is given by the Dirac exchange energy functional [40]. A popular analytical form of the correlation contribution has been given by Vosko, Wilk and Nusair (VWN) [45], others are due to Perdew and Zunger (PZ81)

[46] and Perdew and Wang (PW92) [47]. For practical purposes all LDA functionals are next to equivalent.

More recently, however, these approximations to E_{xc} have been much improved by the introduction of the generalized gradient approximation (GGA), which supplements the LDA term with one that depends explicitly on the gradients of the density,

$$E_{xc}^{GGA}[\rho(\vec{r})] = \int d\vec{r} F_{xc}(\rho(\vec{r}), \vec{\nabla}\rho(\vec{r})). \quad (2.14)$$

It was the advent of GGAs that made DFT popular among chemists since they provided for the first time a level of accuracy, which allows for the quantitative discussion of chemical bonds. Popular gradient corrections are the ones by Becke (B88) [48] and Perdew and Wang (PW86) [49] for the exchange contribution and the ones by Perdew (P86) [50], Becke (B88C) [51], and Lee, Yang and Parr (LYP) [52] for the correlation contribution. Perdew et al. (PW91) [53], Perdew, Burke and Wang (PBW96) [54] and Perdew, Burke and Ernzerhof (PBE) [55] have given widely used expressions for the complete XC energy. In this work the exchange correlation effects are modeled using PBE function at the level of GGA.

2.2 Basis set methods

Although in principle the MOs can be represented on a grid and the KS equations solved numerically, in molecular calculations the MOs are in general expanded into a set $\{\phi_{\mu}\}$ of atom-centered basis functions or atomic orbitals (AOs) according to

$$\psi_i(\vec{r}) = \sum_{\mu} C_{\mu}^i \phi_{\mu}(\vec{r}). \quad (2.15)$$

Within this linear combination of atomic orbitals (LCAO) expansion the electron density [Eq. (2.2)] is then given as

$$\rho(\vec{r}) = \sum_{\mu\nu} P_{\mu\nu} \phi_{\mu}(\vec{r}) \phi_{\nu}(\vec{r}), \quad (2.16)$$

where, P is the first order reduced density matrix with elements

$$P_{\mu\nu} = 2 \sum_i^{\text{occ.}} C_{\mu}^i C_{\nu}^i. \quad (2.17)$$

The expression for the total electronic energy [Eq. (2.1)] now reads as

$$E = \sum_{\mu\nu} P_{\mu\nu} \langle \phi_{\mu} | -\frac{\nabla^2}{2} + v_{\text{ext}}(\vec{r}) | \phi_{\nu} \rangle + \frac{1}{2} \sum_{\mu\nu\kappa\lambda} P_{\mu\nu} P_{\kappa\lambda} \iint d\vec{r}_1 d\vec{r}_2 \phi_{\mu}(\vec{r}_1) \phi_{\nu}(\vec{r}_2) r_{12}^{-1} \phi_{\kappa}(\vec{r}_1) \phi_{\lambda}(\vec{r}_2) + E_{\text{xc}}[\rho(\vec{r})] \quad (2.18)$$

The variational parameters in this energy expression are the MO coefficients or the elements of the density matrix and application of the variational principle leads to the matrix eigenvalue equation

$$H^{\text{KS}} C = S C \varepsilon \quad (2.20)$$

instead of the operator equation (2.10). In Eq. (2.20) H^{KS} is the matrix representation of the KS operator (2.11) in the AO basis,

$$H_{\mu\nu}^{\text{KS}} = \langle \phi_{\mu} | \hat{H}^{\text{KS}} | \phi_{\nu} \rangle, \quad (2.21)$$

S is the overlap matrix with elements $S_{\mu\nu} = \langle \phi_{\mu} | \phi_{\nu} \rangle$, and the matrix C contains as the MO coefficients C_{μ}^i which are obtained by solving the KS equation (2.20). The matrix ε of the Lagrange multipliers for the orthonormality constraints is a diagonal elements which can be identified with the KS matrix in the canonical MO basis and

its diagonal elements represent the corresponding MO energies ε_i of the KS orbitals Ψ_i .

2.3 Computational details

Our density functional based calculations were carried out using the Naval Research Laboratory Molecular Orbital Library (NRLMOL) package [56-63]. In this package the Kohn–Sham molecular orbitals are expressed as a linear combination of Gaussian-type functions. The Gaussian exponents are optimized for each atom. The basis for the Zn consists of *7s*, *5p*, and *4d* type contracted Gaussians. These contracted Gaussians for Zn are constructed from a set of 20 primitive Gaussians. The exponents of the primitive Gaussian functions ranged from 5.0×10^6 to 5.5×10^{-2} . For the sulfur atom, the number of contracted Gaussians is 6 s-type, 5 p-type, and 3d-type functions contracted from a set of 17 primitive Gaussian functions. The exponents of the Gaussians used for the S atom varies ranges from 6.7×10^5 to 7.1×10^{-2} . The basis set used in the NRLMOL code are optimized for the given atom. In the present calculation the exchange-correlation effects are described within the generalized gradient approximation (GGA) due to Perdew, Burke, and Ernzerhof [55]. This code uses a grid which is optimized for accuracy of the integrals involving Gaussian functions [56]. The Poisson equation is solved analytically. The calculations are carried out at the all-electron level and the geometry optimizations were carried out using the limited-memory Broyden-Fletcher-Goldfarb-Shanno (LBFGS) method. The geometries of the clusters were optimized till the forces dropped below 0.001

Hartree/Bohr. The optimized geometry of the neutral cluster was taken as the starting geometry for the optimization of the charged clusters.

The optimized structures were further examined for vibrational instabilities. The vibrational frequencies are calculated by displacing each atom from its equilibrium positions and calculating the forces. For a molecule with N atoms with C1 symmetry this leads to 6N SCF calculations. The dynamical matrix can be constructed from the forces of the perturbed system using a finite difference approximation. From this matrix the frequencies are calculated. The infrared and Raman spectra are calculated by applying a small electric field of 0.005 a.u. The details of these methods can be found in Ref. [63].

2.4 General rules concerning vibrations [64]

- If two oscillators with different frequencies are coupled, then the low frequency is shifted to a lower value, the high frequency to a higher value. This effect is more pronounced the smaller the difference between the original frequencies is.
- If in a molecule n oscillators of the same frequency are coupled, then there are different stretching normal vibrations in which all oscillators participate, but with different phases.
- All normal vibrations are symmetric or anti-symmetric with respect to the symmetry operations on the molecule.
- According to Rayleigh's rule if in a vibrating system any mass is increased or any force constant is reduced, then vibrational frequencies are either reduced or they remain constant, but no frequency is increased.

- There are two main types of vibrations. Those which change bond lengths are called stretching vibrations and those which change bond angles are bending and torsional vibrations. Bending vibrations deform mainly bond angles at one atom, while torsional vibrations change the dihedral angle between planes defined by the ligands at both atoms of a bond.
- The number of vibrational degrees of freedom of a non-linear molecule with n atoms is

$$f = 3n - 6 \quad (2.4.1)$$

while for a linear molecule this number is

$$f = 3n - 5 \quad (2.4.2)$$

For a non-linear and noncyclic molecule with b chemical bonds, the number of stretching degrees of freedom is (Decius, 1949):

$$n_b = b \quad (2.4.3)$$

The number of bending degrees of freedom is

$$n_{\square} = 4b - 3n + n_1 \quad (2.4.4)$$

Here, n_1 is the number of singly bonded (terminal) atoms.

The number of torsions is equivalent to the number of non-terminal bonds:

$$n_{\tau} = b - n_1 \quad (2.4.5)$$

- The observed normal vibrations are a linear combination of these degrees of freedom.
- An overtone (of a deformation) vibration of the same frequency as a fundamental (stretching) vibration of the same bonds may mix with the fundamental to produce two bands of nearly equal intensity. This effect, which may produce supernumerary bands of nearly equal intensity. This effect, which may produce supernumerary bands, is called Fermi resonance.

2.5 IR Spectroscopy

The infrared portion of the electromagnetic spectrum is divided into three regions; the near-, mid- and far- infrared, named for their relation to the visible spectrum. The far-infrared, approximately $400\text{--}10\text{ cm}^{-1}$ ($1000\text{--}30\text{ }\mu\text{m}$), lying adjacent to the microwave region, has low energy and may be used for rotational spectroscopy. The mid-infrared, approximately $4000\text{--}400\text{ cm}^{-1}$ ($30\text{--}1.4\text{ }\mu\text{m}$) may be used to study the fundamental vibrations and associated rotational-vibrational structure. The higher energy near-IR, approximately $14000\text{--}4000\text{ cm}^{-1}$ ($1.4\text{--}0.8\text{ }\mu\text{m}$) can excite overtone or harmonic vibrations. The names and classifications of these sub regions are merely conventions. They are neither strict divisions nor based on exact molecular or electromagnetic properties.

Infrared spectra are usually recorded by measuring the transmittance of light quanta with a continuous distribution of the sample. The frequencies of the absorption bands ω_s are proportional to the energy difference between the vibrational ground and excited states. The absorption bands due to the vibrational transitions are found in the

wavelength region of $\lambda = 2.5 \dots 1000 \mu\text{m}$, which is equivalent to $\tilde{\nu} = 4000 \dots 10 \text{ cm}^{-1}$. There are $k = 3n - 6$ normal vibrations of a non-linear molecule with n atoms. These vibrations may absorb infrared radiation only if they modulate the molecular dipole moment μ_k , which is a vector with components μ_x , μ_y , and μ_z .

$$\mu_k = \mu_0 + (d\mu / dq_k)_0 + (1/2)(d^2\mu/dq_k^2)_0 q_k^2 + \dots \quad (2.5.1)$$

The macroscopic and molecular properties are related by the integral Napierian absorption coefficient. The integral Napierian absorption coefficient of the k^{th} normal is given by

$$A_k = (N_1 \pi / 3 c) [(d\mu_x/dq_k)_0^2 + (d\mu_y/dq_k)_0^2 + (d\mu_z/dq_k)_0^2], \quad (2.5.2)$$

in which, N_1 is the number of molecules per cm^3 .

Infrared spectroscopy exploits the fact that molecules have specific frequencies at which they rotate or vibrate corresponding to discrete energy levels (vibrational modes). These resonant frequencies are determined by the shape of the molecular potential energy surfaces, the masses of the atoms and, by the associated vibronic coupling. In order for a vibrational mode in a molecule to be IR active, it must be associated with changes in the permanent dipole. In particular, in the Born-Oppenheimer and harmonic approximations, i.e. when the molecular Hamiltonian corresponding to the electronic ground state can be approximated by a harmonic oscillator in the neighborhood of the equilibrium molecular geometry, the resonant frequencies are determined by the normal modes corresponding to the molecular electronic ground state potential energy surface. Nevertheless, the resonant frequencies can be in a first approach related to the strength of the bond, and the mass of

the atoms at either end of it. Thus, the frequency of the vibrations can be associated with a particular bond type.

Simple diatomic molecules have only one bond, which may stretch. More complex molecules have many bonds, and vibrations can be conjugated, leading to infrared absorptions at characteristic frequencies that may be related to chemical groups. For example, the atoms in a CH₂ group, commonly found in organic compounds can vibrate in six different ways: symmetrical, anti symmetrical stretching, scissoring, rocking, wagging and twisting:

The infrared spectrum of a sample is collected by passing a beam of infrared light through the sample. Examination of the transmitted light reveals how much energy was absorbed at each wavelength. This can be done with a monochromatic beam, which changes in wavelength over time, or by using a Fourier transform instrument to measure all wavelengths at once. From this, a transmittance or absorbance spectrum can be produced, showing at which IR wavelengths the sample absorbs. Analysis of these absorption characteristics reveals details about the molecular structure of the sample.

This technique works almost exclusively on samples with covalent bonds. Simple spectra are obtained from samples with few IR active bonds and high levels of purity. More complex molecular structures lead to more absorption bands and more complex spectra. The technique has been used for the characterization of very complex mixtures.

Infrared spectroscopy is widely used in both research and industry as a simple and reliable technique for measurement, quality control and dynamic measurement. It is of

especial use in forensic analysis in both criminal and civil cases, enabling identification of polymer degradation for example. It is perhaps the most widely used method of applied spectroscopy. By measuring at a specific frequency over time, changes in the character or quantity of a particular bond can be measured. This is especially useful in measuring the degree of polymerization in polymer manufacture. Modern research machines can take infrared measurements across the whole range of interest as frequently as 32 times a second. This can be done whilst simultaneous measurements are made using other techniques. This makes the observations of chemical reactions and processes quicker and more accurate. Infrared spectroscopy has been highly successful for applications in both organic and inorganic chemistry. Infrared spectroscopy has also been successfully utilized in the field of semiconductor microelectronics: for example, infrared spectroscopy can be applied to semiconductors like silicon, gallium arsenide, gallium nitride, zinc selenide, amorphous silicon, silicon nitride, etc.

2.6 Raman spectroscopy

Raman spectroscopy is used in condensed matter physics and chemistry to study vibrational, rotational, and other low-frequency modes in a system. It relies on inelastic scattering, or Raman scattering of monochromatic light, usually from a laser in the visible, near infrared, or near ultraviolet range. The laser light interacts with phonons or other excitations in the system, resulting in the energy of the laser photons being shifted up or down. The shift in energy gives information about the phonon modes in the system. Infrared spectroscopy yields similar, but complementary information.

Typically, a sample is illuminated with a laser beam. Light from the illuminated spot is collected with a lens and sent through a monochromator. Wavelengths close to the laser line, due to elastic Rayleigh scattering, are filtered out while the rest of the collected light is dispersed onto a detector.

Spontaneous Raman scattering is typically very weak, and as a result the main difficulty of Raman spectroscopy is separating the weak inelastically scattered light from the intense Rayleigh scattered laser light. There are a number of advanced types of Raman spectroscopy, including Surface enhanced Raman, polarized Raman, stimulated Raman (analogous to stimulated emission), Transmission Raman, Spatially offset Raman and Hyper Raman.

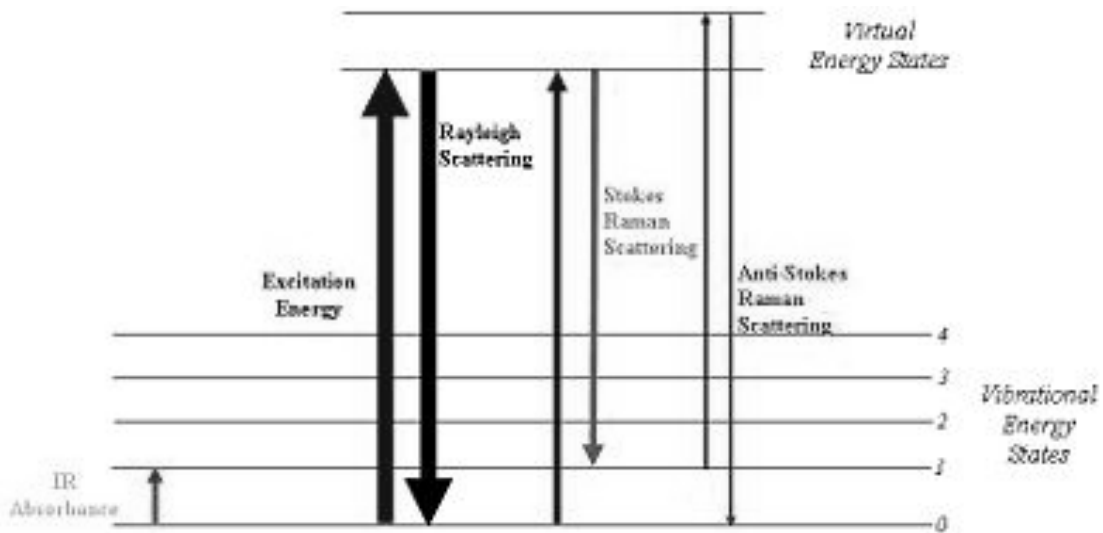


Figure 2.5.1 Energy level diagram of Raman signal

Figure 2.5.1 is energy level diagram showing the states involved in Raman signal. The line thickness is roughly proportional to the signal strength from the different transitions.

The Raman Effect occurs when light impinges upon a molecule and interacts with the electron cloud of the bonds of that molecule. The incident photon excites one of the electrons into a virtual state. For the spontaneous Raman Effect, the molecule will be excited from the ground state to a virtual energy state, and relax into a vibrational excited state, which generates Stokes Raman scattering. If the molecule was already in an elevated vibrational energy state, the Raman scattering is then called anti-Stokes Raman scattering.

A molecular polarizability change or amount of deformation of the electron cloud, with respect to the vibrational coordinate is required for the molecule to exhibit the Raman Effect. The amount of the polarizability change will determine the Raman scattering intensity, whereas the Raman shift is equal to the vibrational level that is involved.

When quanta of the energy $h\nu_0$ hit the molecule, an elastic impact scatters the quantum $h\nu_0$, inelastic impacts scatter quanta which have energies smaller or larger by the amount of the vibrational energy, $h\nu_s$. The irradiation with light quanta $h\nu_0$ of molecules in the vibrational ground state may lead to molecules in the vibrational excited state, quanta with energy $h\nu_R^- = h\nu_0 - h\nu_s$ are scattered. Since some molecules are according to Boltzmann law already in the excited state, also in the process emission is possible which produces quanta of larger energy, $h\nu_R^+ = h\nu_0 + h\nu_s$. Therefore in Raman spectrum two lines are seen, which differ from the frequency of the exciting radiation by the vibrational frequency. The Raman line with the lower frequency (the Stokes line) is stronger, that with the larger frequency (the anti-Stokes line) weaker. Their intensity ratio is given by the ratio of the occupancies of both levels.

Raman spectroscopy is commonly used in chemistry, since vibrational information is very specific for the chemical bonds in molecules. It therefore provides a fingerprint by which the molecule can be identified. The fingerprint region of organic molecules is in the range $500\text{-}2000\text{ cm}^{-1}$. For instance, the vibrational frequencies of SiO , Si_2O_2 , and Si_3O_3 were identified and assigned on the basis of normal coordinate analyses using infrared and Raman spectra. Another way that the technique is used is to study changes in chemical bonding, e.g., when a substrate is added to an enzyme.

Raman gas analyzers have many practical applications. For instance, they are used in medicine for real-time monitoring of anesthetic and respiratory gas mixtures during surgery. In solid state physics, spontaneous Raman spectroscopy is used to, among other things, characterize materials, measure temperature, and find the crystallographic orientation of a sample. As with single molecules, a given solid material has characteristic phonon modes that can help an experimenter identify it. In addition, Raman spectroscopy can be used to observe other low frequency excitations of the solid, such as plasmons, magnons, and superconducting gap excitations. The spontaneous Raman signal gives information on the population of a given phonon mode in the ratio between the Stokes (downshifted) intensity and anti-Stokes (up shifted) intensity.

Raman scattering by an anisotropic crystal gives information on the crystal orientation. The polarization of the Raman scattered light with respect to the crystal and the polarization of the laser light can be used to find the orientation of the crystal, if the crystal structure (specifically, its point group) is known. Raman active fibers, such as aramid and carbon, have vibrational modes that show a shift in Raman frequency with

applied stress. Polypropylene fibers also exhibit similar shifts. The radial breathing mode is a commonly used technique to evaluate the diameter of carbon nanotubes.

Spatially Offset Raman Spectroscopy (SORS), which is less sensitive to surface layers than conventional Raman, can be used to discover counterfeit drugs without opening their internal packaging, and for non-invasive monitoring of biological tissue. Raman spectroscopy can be used to investigate the chemical composition of historical documents. This is especially helpful because Raman spectroscopy offers a non-invasive way to determine the best course of preservation or conservation treatment for such materials. In nanotechnology, a Raman Microscope can be used to analyze nanowires to better understand the composition of the structures. Raman spectroscopy is being investigated as a means to detect explosives for airport security.

Chapter 3

RESULTS AND DISCUSSION

3.0 Geometrical Structures of Neutral and Singly Charged (Positive & Negative) ZnS Clusters.

In order to obtain the equilibrium geometry for each size we started with several possible geometric configurations. We did not impose any symmetry constraint during the geometry optimization. All structures were optimized until the force on each atom is less than 0.001 Hartree/Bohr. Following optimization, we obtained the vibrational frequencies for all equilibrium structures. The structures with positive frequencies are the real local minima and are called vibrationally stable. Only the structures that are vibrationally stable (local minima) are discussed below. To obtain charged clusters, only the lowest energy neutral geometries were used.

Matxain et al. [10] have earlier investigated the structures of small ZnS clusters for sizes $n=1-9$. They have also found that small clusters of Zn_nS_n up to $n=5$ have ring-like structures. They have used density functional theory with relativistic pseudopotentials with Becke3 exchange potential and Lee-Yang-Perdew correlation potentials (B3LYP). Similar planar structures were also found for Zn_nSe_n , Zn_nTe_n and isoelectronic Cd_nS_n clusters where $n \leq 5$ [11]. On the other hand oxide clusters favors a ring-like structure for larger size also [12]

3.1 ZnS

The ZnS dimer is bound to be a linear structure. The bond length of the neutral molecule is 2.07 Ang. This is smaller than the bond-length in bulk by 12% mainly due to the reduced coordination of both the Zn and S atoms. Also our calculated bond length is

only slightly smaller than that of Matxain et al [8-12] who found the bond-length to be 2.09 Ang. The bond length increases in the charged states. The bond length of the cation structure increases by 0.09 Ang whereas in the anion structure it increases by 0.08 Ang.

The calculated dipole moment obtained for neutral ZnS dimer is 16.76×10^{-30} C-m. The Zn-S bond length is 2.07×10^{-10} m. Therefore the charge on the Zn or S atom is $q = 16.76 \times 10^{-30} / 2.07 \times 10^{-10} = 8.105 \times 10^{-20}$ C. The percentage of ionicity is then $8.105 \times 10^{-20} \times 100 / 1.602 \times 10^{-19} = 50.6\%$. Therefore the bond can be considered to be partly ionic and partly covalent.

The electron affinity of the ZnS dimer is 2.26 eV and its first ionization potential is 8.74 eV. The vertical ionization potential is only 0.02 eV higher than the adiabatic value. The binding energy of the ZnS dimer is 2.65 eV. From this energetics it can be concluded that ionization of the ZnS dimer which requires 8.74 eV, will lead to a dissociation of the ZnS bond which requires only 2.65 eV to dissociate. This also indicates that due to the high probability of dissociation, observation or peaks related to ZnS dimer in experiments where the clusters are ionized such as IR-REMPI, mass spectroscopy etc. will be small. Indeed, it was found by Burnin et al. [65] from their laser ablation experiments on the formation of ZnS clusters using a mixture of zinc powder and sulfur powder, that the peak for ZnS⁺ in time of flight mass spectrum is quite small compared to others and also depends on the ratio of Zn to S powder in the mixture. However, laser ablation of ZnS bulk did show a larger peak.

3.2 Zn₂S₂:

We have found four vibrationally stable isomers of Zn₂S₂. All the structures are of planar form. The lowest energy structure 2a is like a rhombus with Zinc atoms on two opposite corners of the rhombus and sulfur atoms on the other two opposite corners. The structure of 2a is shown in Figure 3.2.1. The Zn-S bond length is 2.25 Ang and S-Zn-S bond angle is 114.6°. In this case also, our calculated bond length is only slightly smaller than the B3LYP value of 2.27 Ang [10]. As the coordination of the Zn and S increases, the bond length also increases. However, a clear trend can not be observed from the average bond lengths of these small clusters (Table 3.8.2). The dipole moment of this symmetric cluster is negligible.

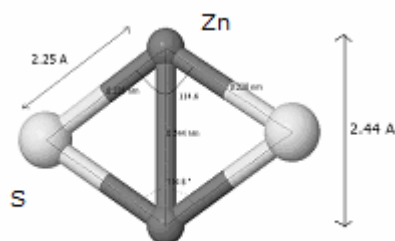


Fig. 3.2.1 lowest energy structure 2a

The next lowest energy structure which is vibrationally stable is 2b having similar geometric structure as of 2a but with the positions of Zn and S atoms interchanged. The structure of 2b is shown in Figure 3.2.2. This structure is higher in energy by 1.83 eV.

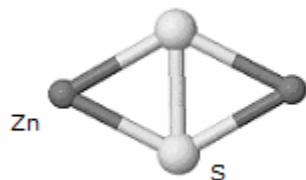


Figure 3.2.2 Structure 2b

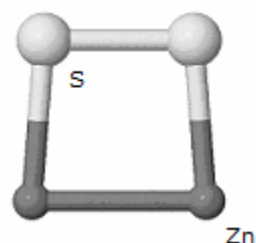


Figure 3.2.3 Structure 2c

Third vibrationally stable structure in this size is 2c. It is like a quadrilateral and has both Zinc atoms on one side and both Sulfur atoms on another side. Zn-S bond length in 2c is larger than the Zn-S bond lengths of 2a and 2b. The 2c isomer lies 1.15 eV higher in energy compared to the structure 2a. The structure of 2c is shown in Figure 3.2.3. Since both the isomers of Zn_2S_2 lie much higher in energy, at room temperature the probability of observing these isomers is negligible.

The bond angle S-Zn-S for 2a is greater than the bond angle S-Zn-S of 2b indicating that the more stable structure prefers Zn-Zn distance lesser than the S-S distance. The relaxed cation structure is shown in Figure 3.2.4.

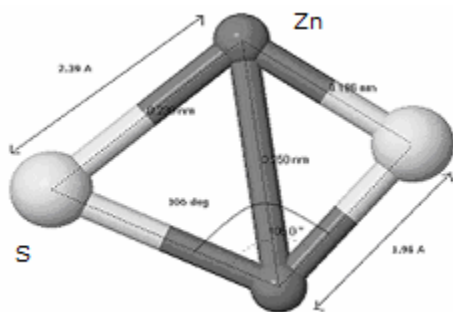


Figure 3.2.4 Relaxed Cation of $Zn_2S_2^+$

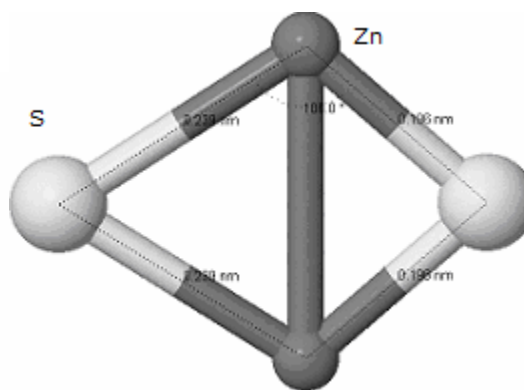


Figure 3.2.5 Relaxed anion of $Zn_2S_2^-$

In the relaxed cation structure $Zn_2S_2^+$, the Zn-S distance has decreased by 0.29 Å on one side and increased by 0.14 Å on the other side than the neutral stable structure 2a.

As the result, the distances between Zn-Zn and S-S have increased and the nearly symmetric structure of the neutral cluster is lost. The vertical IP of the Zn_2S_2 is 8.50 eV. Relaxation of the cation leads to a structure that is 8.28 eV above the neutral cluster. In the Zn_2S_2 cluster the binding energy per ZnS unit is 4.72 eV and therefore the cluster is energetically stable against dissociation through ionization. In fact this feature is observed in all larger ZnS clusters studied here as can be seen from table 3.8.2. The vertical electron affinity of the 2a structure is 1.72 eV and the adiabatic electron affinity is 1.91 eV. Relaxed anion structure is shown in Figure 3.2.5.

3.3 Zn_3S_3

The lowest energy structure 3a has a ring like triangular form with S atoms at the corners of the triangle and Zn atoms at the middle of the sides of the triangle. This structure is shown in Figure 3.3.1.

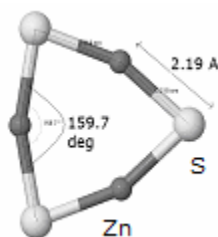


Figure 3.3.1 Stable structure 3a

In comparison with ZnS dimer and Zn_2S_2 structures the Zn-S bond distance is approximately the average of the two and the bond angle S-Zn-S is more than the bond angle S-Zn-S of 2a. The relaxed structures of the cation and anion of 3a are shown in Figure 3.3.2 and Figure 3.3.3 respectively.

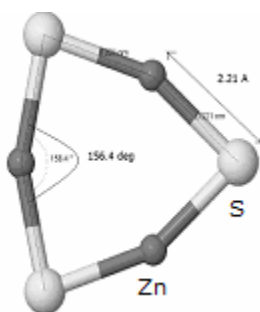


Fig.3.3.2 Relaxed cation of Zn_3S_3 .

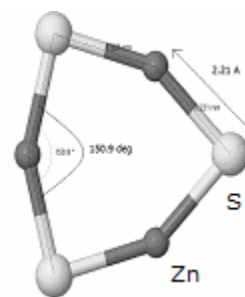


Fig. 3.3.3 Relaxed anion of Zn_3S_3 .

In the relaxed cation structure, Zn-S distance has increased by 0.02 Ang than the neutral 3a structure. This is evident from the relaxed ZnS^+ structure which shows an increase in the bond distance by 0.09 Ang. The decrease in the bond angle S-Zn-S in the relaxed cation can be attributed to the increase in the Zn-S bond length.

The bond length of the relaxed anion (Fig. 3.3.3) has increased and the bond angle S-Zn-S has decreased. This effect in the cation and anion may be due to effect of unshared pairs on bond lengths.

3.4 Zn_4S_4

Five structures of Zn_4S_4 cluster were optimized and all the isomers are vibrationally stable. The lowest energy structure 4a is a planar square-like structure with four Sulfur atoms at the four corners of the square and the four Zinc atoms at the middle of each side. Figure 3.4.1 gives structure of 4a.

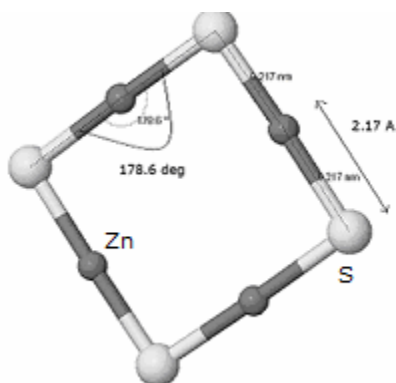


Figure 3.4.1 Structure 4a

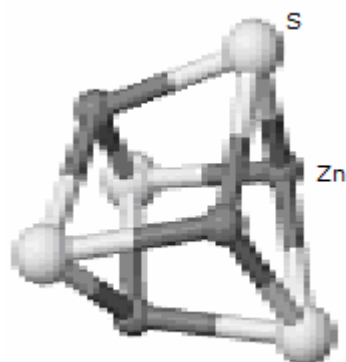


Fig. 3.4.2 Isomer 4b.

The next isomer in this size is 4b that has a cubane-like 3D structure and can be viewed as a fusion of two 2a structures. The fused 2a clusters are rotated such that Zn in one plane faces S in the other plane. The structure 4b is shown in Figure 3.4.2.

The next low-lying is 4c and is shown in Figure 3.4.3. It has a three-dimensional structure and looks close to the arrangement of atoms of the zinc blend structure. It has a minimum Zn-S bond distance of 2.13 Ang which is smaller than the 4a structure.

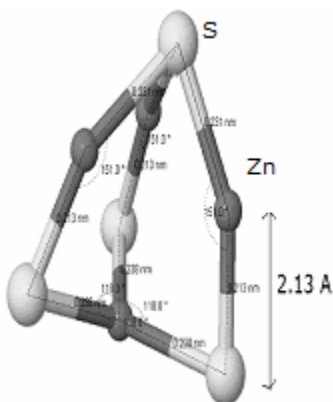


Figure 3.4.3 Isomer 4c

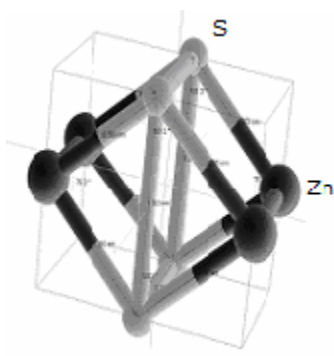


Fig. 3.4.4 Isomer 4d

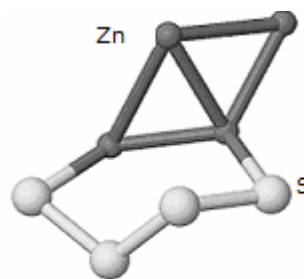


Fig. 3.4.5 Isomer 4e

The next in this series is structure 4d which is similar to 4c structure except that the Zn atoms face Zn in the opposite plane and S atoms face S atoms in the opposite plane. The 4d structure is shown in Figure 3.4.4.

An entirely different structure in this series is 4e. In this isomer, all four atoms of Zn are in one plane forming a quadrilateral with none of the S atoms in this plane. The S atoms are arranged as a chain. The structure is shown in Figure 3.4.5.

The isomers of the Zn_4S_4 are quite high in energy compared to the energy of the 4a structure. The 4b and 4c structures lay 0.80 and 1.7 eV higher in energy. The 4d and 4e are 4.6 and 5.7 eV higher than 4a, respectively. This is not surprising since these clusters have fewer ZnS bonds. The probability of observing all these clusters in experiments is vanishingly small. Thermal excitation to these structures is not achievable under normal laboratory conditions.

The relaxed cation $Zn_4S_4^+$ and relaxed anion $Zn_4S_4^-$ structures are given in Figure 3.4.6. In Figure 3.4.6 the Zn-S bond length has increased by 0.02 Ang and the bond angle has decreased which is in agreement with the previous lower size relaxed cationic structures.

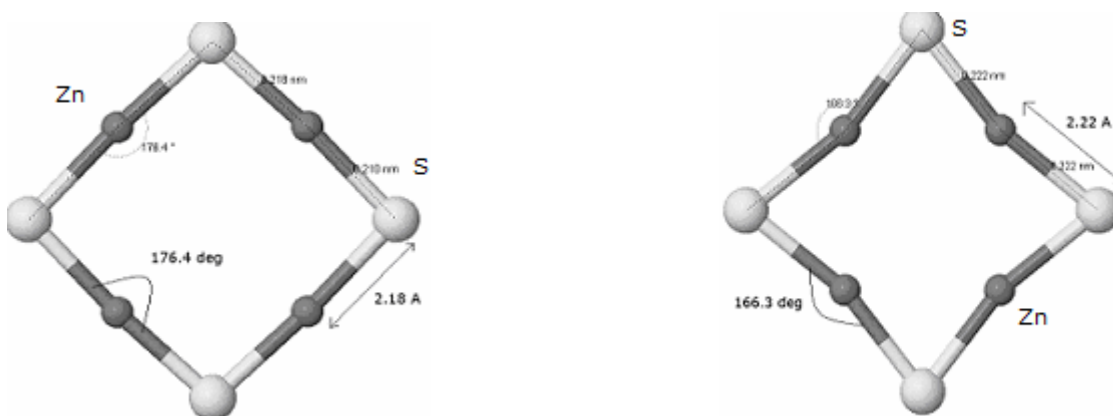


Figure 3.4.6 Relaxed geometries of the cation and anion of 4a structure.

In the relaxed anion $Zn_4S_4^-$ structure there is an increase in the bond length as expected but the Zn atoms have buckled inside and the bond angle has decreased. Also it is puzzling to see that the $Zn_4S_4^-$ relaxed structure has Zn atoms closer than the Zn atoms in

$Zn_4S_4^+$ and Zn_4S_4 structures. The closest distance between the Zn atoms in 4a is about 3.11 Ang. and that in the relaxed anion is about 2.75 Ang.

3.5 Zn_5S_5

For this size two structures were optimized but only one structure is vibrationally stable. The stable structure 5a is planar ring- like pentagon structure with Sulfur atoms at the corners of the pentagon and Zinc atoms at the middle of the sides. The structure 5a is shown in Figure 3.5.1.

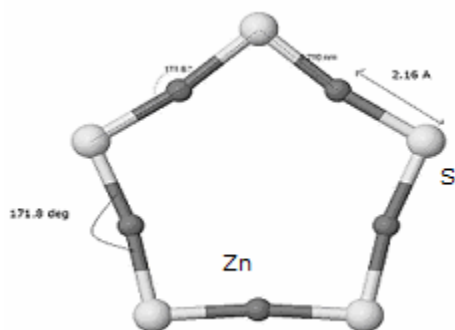


Figure 3.5.1 lowest energy structure 5a

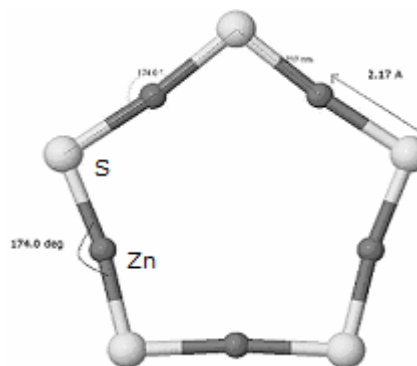


Fig. 3.5.2 Relaxed Cation of Zn_5S_5

Relaxed structure of the cation $Zn_5S_5^+$ is shown in Figure 3.5.2. Bond lengths in the relaxed cation $Zn_5S_5^+$ have followed the path of the smaller sizes. An interesting result is that the bond angle S-Zn-S has increased instead of decreasing as in the case of smaller sizes. Since the Zn atoms have to move away the increment in the angle is justified. The relaxation of the cation is small as shown by the small difference of the vertical and adiabatic ionization potentials (Table 3.7.2).

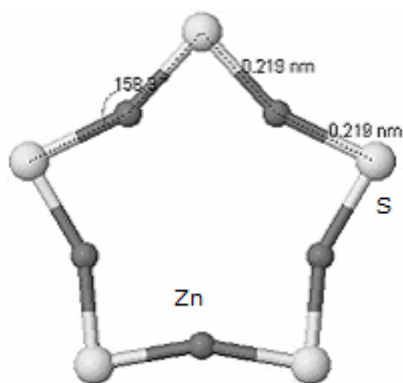


Fig. 3.7.3 Relaxed anion of Zn_5S_5

The relaxed anion structure is shown in Fig. 3.7.3. The bond distance Zn-S has increased and the bond angle S-Zn-S has decreased moving the Zn atoms away and in agreement with the lower size structures.

3.6 Zn_6S_6 :

We found only one vibrationally stable structure. The structure 6a is a three dimensional structure with two planes of triangular rings similar to 3a but one plane rotated such that Zn atoms in one plane face S atoms in the other plane. In both the planes the Sulfur atoms occupy the corners and Zn atoms are at the middle of the sides. This is first lowest energy structure in the series which is three dimensional. The Zn-S bond length in this structure is 2.29 Ang which is close to that of the bulk ZnS (which is about 2.34 Ang). The structure 6a is shown in Figure 3.6.1. Both the Zn and S atoms in 6a are coordinated with three atoms of opposite kind. The increased coordination has led to increase in the binding energy. This cluster also has larger vertical electron affinity (1.81 eV) compared to the smaller members of the series except the dimer. It may be pointed out here that for Zn_6O_6 a planar ring-like structure is predicted to be the most stable structure by Khanna and his coworkers using DFT [66]. However, they found that Zn_8O_8

has a 3D structure similar to our Zn_6S_6 structure but with two more units. Due to the high symmetry of the structure, the dipole moment of Zn_6S_6 is vanishingly small.

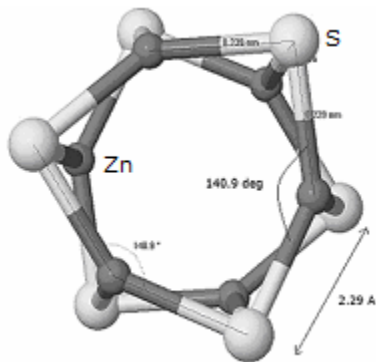


Figure 3.6.1 Stable structure 6a

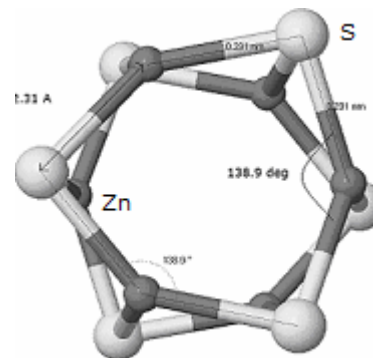


Fig. 3.6.2 Relaxed anion of Zn_6S_6

Relaxed anion $Zn_6S_6^-$ structure is given in Figure 3.6.2. The optimization of the cation structure for this size did not converge during the time of the project. As expected the bond length has increased and the bond angle decreased in the relaxed structure forcing the Zn atoms to move away from each other.

3.7 Data on the structural and electronic properties

Table 3.7.1 gives the comparative distances between atoms in the clusters. We have observed that in all the lowest energy structures of the Zn_nS_n clusters studied here, the S-S distances are larger than the Zn-Zn distances. Table 3.7.2 gives the complete data on the Zn-S clusters about their bond lengths, bond angles, binding energies per ZnS unit, HOMO-LUMO gaps, vertical I.P., adiabatic I.P. and electron affinities. Table 3.7.3 gives the difference of energies of isomers of ZnS clusters.

Table 3.7.1 Comparative distances of the Atoms in the ZnS Clusters

Structure	Comparative distances between atoms
2a	S-S > Zn-Zn > Zn-S
2b	Zn-Zn > Zn-S > S-S
2c	Zn-S > Zn-Zn > S-S
3a	S-S > Zn-Zn > Zn-S
4a	S-S > Zn-Zn > Zn-S
4b	S-S > Zn-Zn > Zn-S
4c	S-S > Zn-Zn > Zn-S
4d	Zn-Zn > S-S > Zn-S
5a	S-S > Zn-Zn > Zn-S
6a	S-S > Zn-Zn > Zn-S

Table 3.7.2 Structural and Electronic Properties of ZnS Clusters

	Zn-S Bond length in Ang.	S-Zn-S Bond Angle in degrees	Binding Energy per ZnS unit in eV	HOMO -LUMO gap in eV	Vertical I.P. in eV	Adiabatic I.P. in eV	Vertical Electron Affinity in eV	Adiabatic Electron Affinity in eV
Zn ₁ S ₁	2.07	180	2.65	0.46	8.76	8.74	2.26	2.2
Zn ₂ S ₂	2.25	114.7	4.72	1.55	8.50	8.28	1.72	1.91
Zn ₃ S ₃	2.19	158.6	5.64	2.99	8.51	8.48	1.28	1.48
Zn ₄ S ₄	2.17	178.6	5.62	2.99	8.11	8.10	1.18	1.79
Zn ₅ S ₅	2.16	171.8	5.82	1.12	8.01	7.99	1.44	2.02
Zn ₆ S ₆	2.29	172.7	6.02	2.64	8.08		1.81	1.85

Table: 3.7.3 Energy differences of isomers of ZnS clusters

	Difference between Minimum energy cluster and other local minima in eV
E _{2b} - E _{2a}	1.83
E _{2c} - E _{2a}	1.15
E _{4b} - E _{4a}	0.80
E _{4c} - E _{4a}	1.77
E _{4d} - E _{4a}	4.56
E _{4e} - E _{4a}	5.65

3.8 HOMO-LUMO gaps:

The energy gaps between the highest occupied molecular orbitals and the lowest unoccupied molecular orbitals (HOMO-LUMO gaps) of the lowest energy optimized structures are given below in Table-3.8.1. It is well-known that the density functional theory underestimates the HOMO-LUMO gaps by about 40%. Therefore the values given in the second row of the table are the DFT values and the third row gives the adjusted values.

Table 3.8.1 HOMO-LUMO gaps of ZnS clusters

Zn ₁ S ₁	Zn ₂ S ₂	Zn ₃ S ₃	Zn ₄ S ₄	Zn ₅ S ₅	Zn ₆ S ₆
0.46 eV	1.55 eV	2.99 eV	2.99 eV	1.12 eV	2.64 eV
0.77 eV	2.58 eV	4.98 eV	4.98 eV	1.87 eV	4.40 eV

The above table shows oscillations of the HOMO-LUMO gaps as a function of the cluster size. While the odd-even oscillations of HOMO-LUMO gaps are observed in metal clusters similar clear oscillation are not seen in case of semiconductor clusters. Unlike metal clusters, semiconductor clusters are closed shell systems with a large enough gap. The small gap of ZnS dimer is a surprise and seems to be an artifact of the DFT exchange-correlation potential. Our calculations at a higher level of theory (Coupled cluster) showed the gap of the dimer to be more than 3 eV. Since the ZnS bulk has a direct gap of 3.64 eV, we expect the smaller clusters to have gaps larger or same order of magnitude. However, for the Zn₅S₅ cluster also we see a much smaller gap compared to the gap of the bulk. The reason may be that the ring-like cluster structures are quite different from the bulk and the LUMO states are found to be sensitive to the surface

variation [67-68]. Matxain et al [9] have earlier performed calculations of the excitation energies of small ZnS clusters using both configuration interaction singles theory and the time-dependent DFT. They found that the excitation energy for ZnS dimer with the CIS method ranges from 1.13 – 1.25 eV depending on the number of basis functions. In case of TDDFT, this energy varies from 0.76 to 0.81 eV. Earlier calculations by Hamad et al. [67] simply adjusted the gap value by using a shift operator whose value relates to the difference between the theoretical band gap and the experimental value for bulk ZnS. Pal et al also used a similar shift operator [68] in their calculation using density functional tight-binding approach for ZnS clusters from size n=4 to 104. Our adjusted values of the band gaps range from 0.77 eV for the dimer to 4.98 eV for n=3 and 4. The larger cluster has smaller gaps. Although there is a lack of experimental values for such small size clusters, Li et al. have observed a band gap of 4.49 eV for ZnS quantum dots of average diameter of 3 nm or less [13].

There are a few applications that are probably suitable for these materials according to their band gaps. Figure 3.8.1 [69] gives the solar spectrum (in Earth's atmosphere) intensity per wavelength as a function of wavelength. For example, the intensity of 5000 Ang wavelength photons is 1000 Watt m⁻² and that of 15000 Ang photons is 375 W/m² and so on in the Earth's Atmosphere.

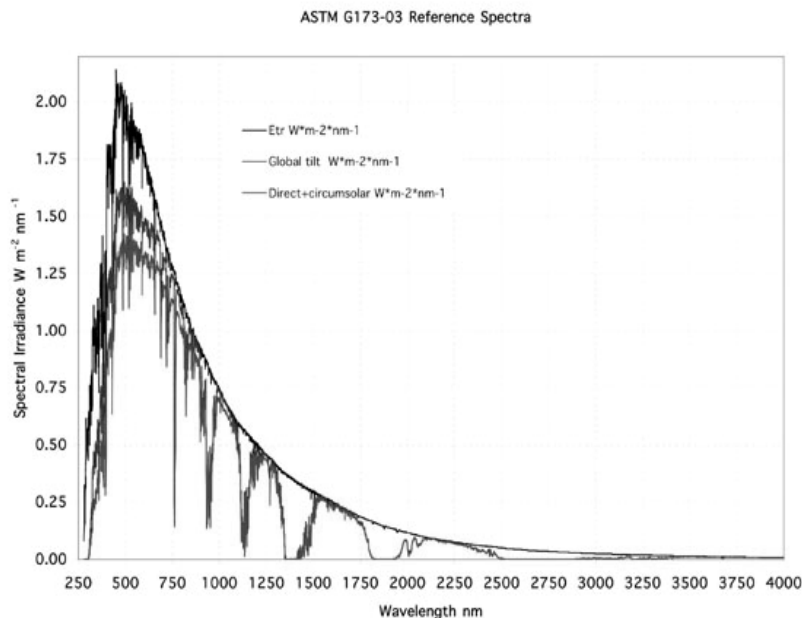


Figure: 3.8.1 Solar Energy per unit wavelength as a function of wavelength.

The maximum intensity of the solar spectrum is in the neighborhood of 5000 Ang which corresponds to the energy of about 2.48 eV. This energy corresponds to visible region. The visible region spreads over the energy range of about 1.8 eV – 3.1 eV (7500 A – 4000 A). Materials with band gaps of this range are probably suitable as Solar cells or photo voltaic cells. This is of course dependent on whether there are dipole allowed transitions at this range. Photo catalysts generally use lower energies in the UV (Ultra Violet) region. UV region corresponds to the energy range of about 3.5 eV – 124 eV (3500 A – 100 A). The material used to make a photodiode is critical to defining its properties, because only photons with sufficient energy to excite electrons across the material's band gap will produce significant photocurrents. Materials commonly used to produce photodiodes include Si, Ge, InGaAs, PbS etc. Based on the band gaps shown by the clusters $Zn_1S_1 - Zn_6S_6$ and the requirements of the above discussed materials we can

probably (considering the band gap only) predict these clusters usage as depicted in Table 3.8.2.

Table 3.8.2 Predictions about usefulness of the small ZnS clusters based on their HOMO-LUMO gaps.

Cluster	Photovoltaic cell	Photo Catalyst	Photo Diode
Zn ₁ S ₁	Useful in visible region	No useful	Useful in visible region
Zn ₂ S ₂	Useful in visible region	Not useful	Useful in visible region
Zn ₃ S ₃	Not useful	May be useful	Not useful
Zn ₄ S ₄	Not useful	May be useful	Not useful
Zn ₅ S ₅	Useful in visible region	Not useful	Useful in visible region
Zn ₆ S ₆	Not useful	May be useful	Not useful

3.9 IR and Raman Spectra

Zn₁S₁

The vibrational mode of Zn₁S₁ has a frequency of 449.5 cm⁻¹. The IR spectrum of Zn₁S₁ is shown in Figure 3.9.1

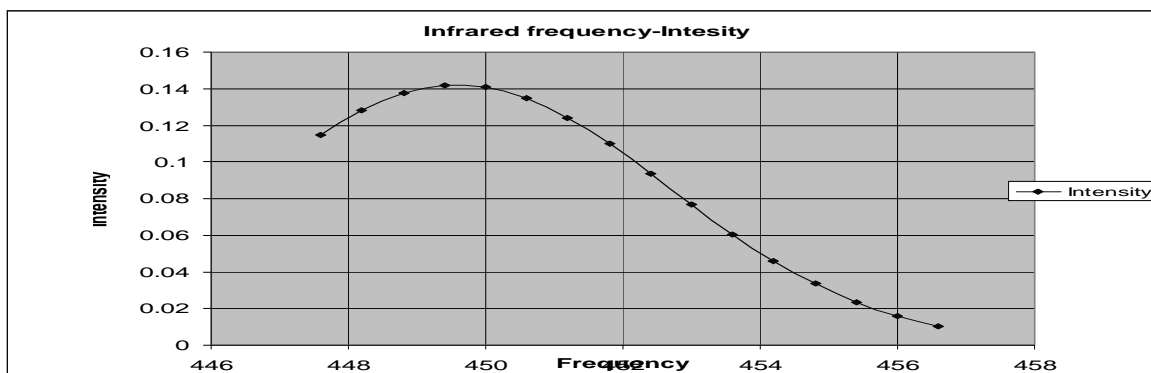


Figure 3.9.1 IR Spectrum of ZnS dimer

The no. of vibrational modes for a linear molecule is given by $3n - 5$. For Zn_1S_1 there is only one mode at 449.5 cm^{-1} . For this mode the value of the spring constant is calculated as

$$k = 4\pi^2c^2\nu^2\mu = 258\text{ N/m} \quad (3.9.1)$$

Where 'c' is the speed of light 'v' is frequency in cm^{-1} and ' μ ' is the reduced mass of the cluster. The ZnS stretch mode is only slightly IR active but shows substantial Raman intensity. Therefore the Raman spectroscopy is a better tool for identification of the ZnS dimer in experiment.

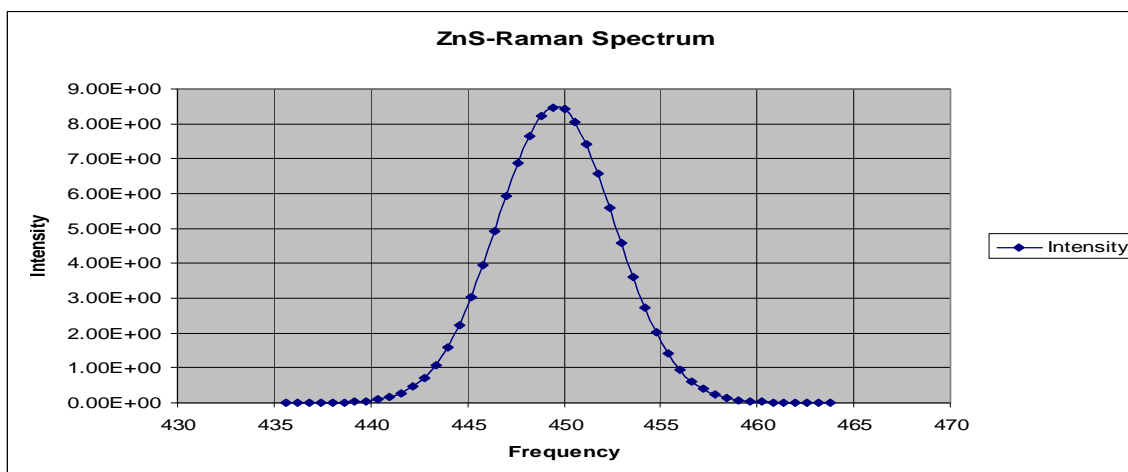


Figure 3.9.2: Raman spectra of ZnS.

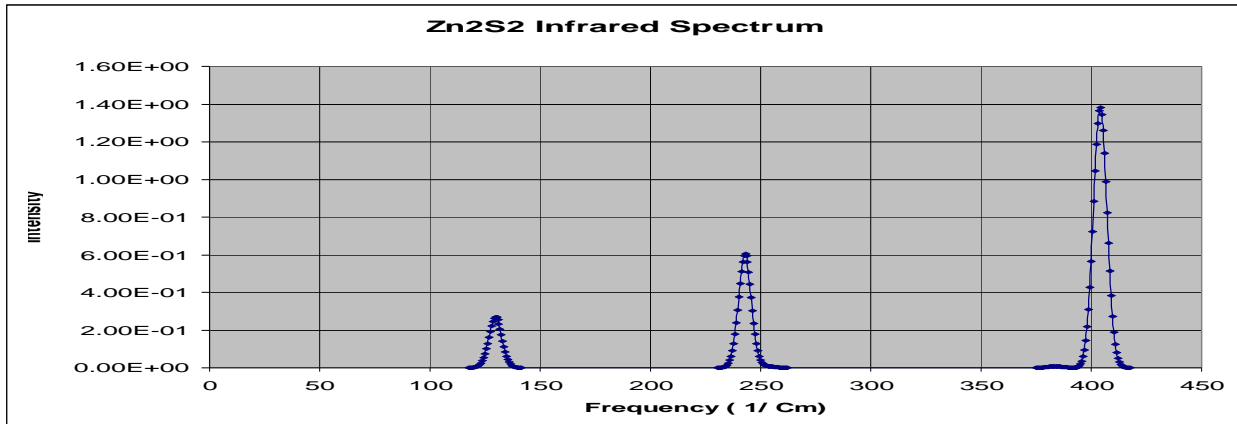


Figure 3.9.3 IR Spectrum of Zn₂S₂

As seen from Figure 3.9.3, the IR Spectrum of Zn₂S₂ has three IR active modes at frequencies 130 cm⁻¹, 240 cm⁻¹ and 405 cm⁻¹. Any non-linear molecule having ‘n’ atoms has 3n degrees of freedom of which only 3n – 6 degrees are motions which change the distances between atoms: the lengths of the chemical bonds and the angles between them. Since Zn₂S₂ has 4 atoms the total number of vibrations possible is 6 of which 3 are IR active and 3 are Raman active. Energy difference between the vibrational ground and excited states for each of the three vibrational modes shown in the IR Spectrum is given as follows.

$$\Delta E = h \nu = h \omega c = 6.6 \times 10^{-34} \times \omega \times 100 \times 3 \times 10^8 / 1.6 \times 10^{-19} = \omega / 8065 \quad (3.10.1)$$

Where ω is expressed in cm⁻¹

$$\Delta E_1 = 130 / 8065 = 0.016 \text{ eV} \quad (3.10.2)$$

$$\Delta E_2 = 240 / 8065 = 0.0298 \text{ eV} \quad (3.10.3)$$

$$\Delta E_3 = 405 / 8065 = 0.0502 \text{ eV} \quad (3.10.4)$$

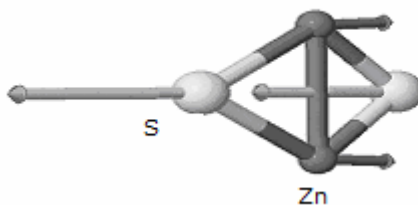


Figure 3.9.4 IR vibration mode of 405 cm^{-1}

Figure 3.9.4 gives the vibration mode for frequency 405 cm^{-1} which shows highest IR activity. It is a stretching vibration as the bond lengths are changing. Based on the above analysis, the vibrational transitions for the lowest mode is possible at room temperature. Raman Spectra of Zn_2S_2 is shown in Figure 3.9.5. It has three active modes at 220 cm^{-1} , 255 cm^{-1} and at 380 cm^{-1} . The mode at 380 cm^{-1} shows highest Raman peak.

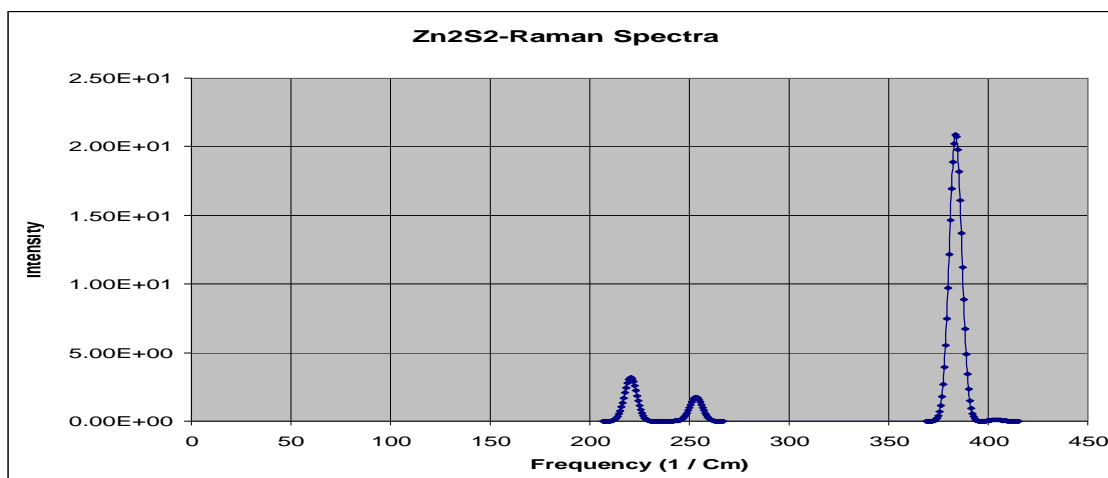


Figure: 3.9.5 Raman Spectrum of Zn_2S_2

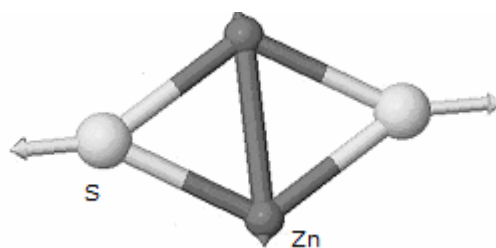


Fig. 3.9.6: Vibrational mode of frequency 380 cm^{-1} which shows a high Raman peak
 The highest frequency of Raman active mode is shown in Figure 3.9.6 and it is a stretching mode of vibration.

Zn₃S₃

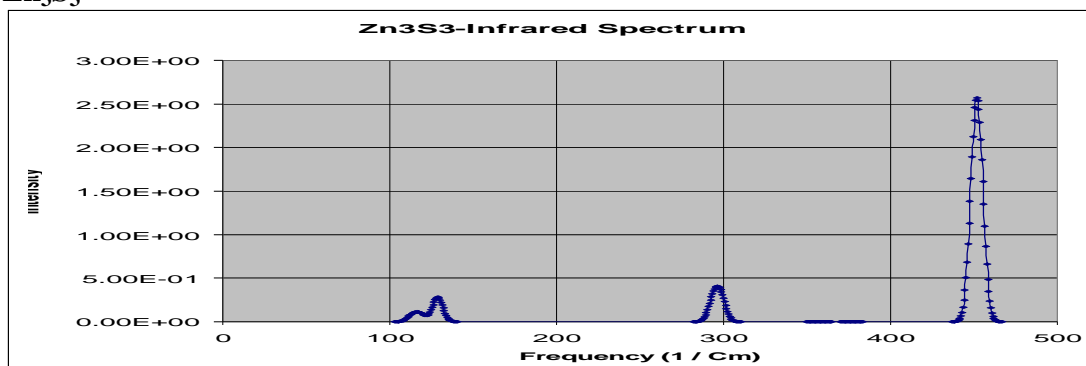


Figure 3.9.7 IR Spectrum of Zn₃S₃

Figure 3.9.7 gives the IR Spectrum of the ring like Zn₃S₃ structure. This structure has $3 \times 6 - 6 = 12$ number of normal modes. We can see 4 IR active vibrations of which one at 450 cm^{-1} is of good intensity and the other three at 110 cm^{-1} , 120 cm^{-1} and 295 cm^{-1} are of low intensity.

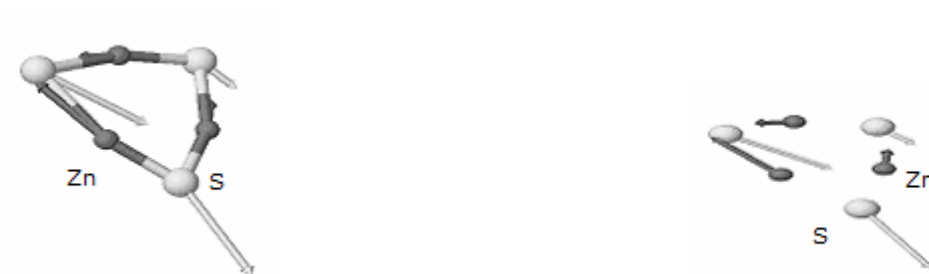


Figure 3.9.8 IR active mode of frequency 449 cm^{-1}

Figure 3.9.8 gives the vibration mode of frequency 449 cm^{-1} which looks like bending and stretching. Figure 3.9.9 shows that Raman spectrum of Zn_3S_3 . Also Zn_3S_3 has 5 Raman active modes of which 360 cm^{-1} is the prominent frequency. The lowest frequency is about 90 cm^{-1} . However the intensities of the other four peaks are much lower compared to the highest peak at 360 cm^{-1} .

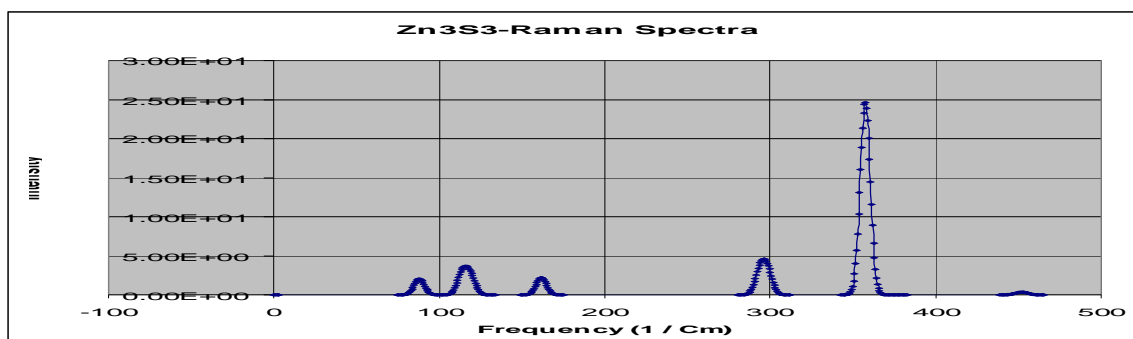


Figure 3.9.9 Raman spectrum of Zn_3S_3 .

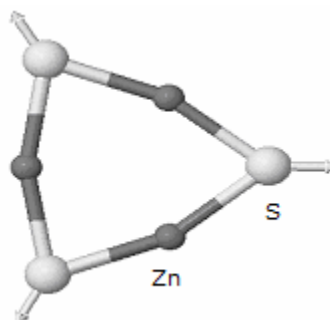


Figure 3.9.10 Raman active mode at 360 cm^{-1}

Figure 3.9.10 shows the Raman mode frequency vibration of 360 cm^{-1} and it is also a breathing mode like the highest Raman mode frequency of Zn_2S_2 .

Zn_4S_4 :

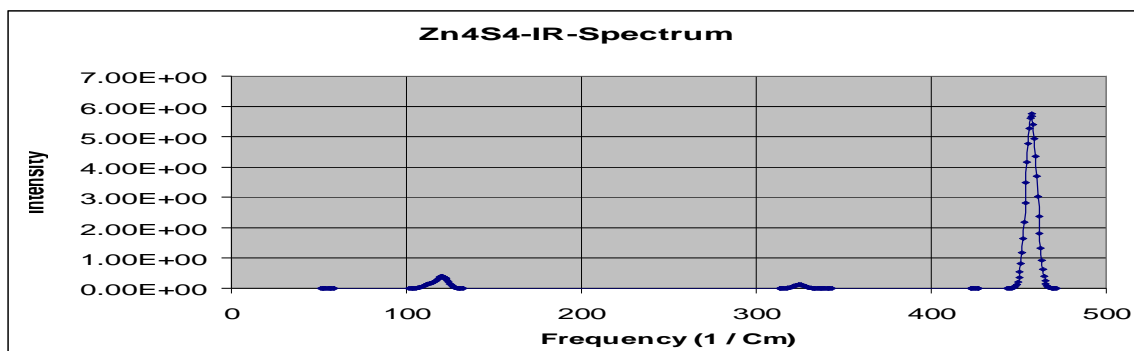


Figure 3.9.11: IR spectrum of Zn_4S_4

Figure 3.9.11 gives the IR Spectrum of Zn_4S_4 . This structure has 18 vibrational modes. But as seen from the Figure only 2 are IR active and only one mode has considerable intensity. The frequencies are of these two modes about 120 cm^{-1} and 455 cm^{-1} .

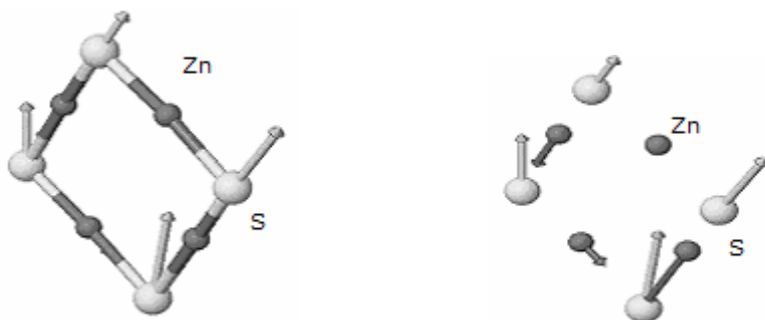


Figure 3.9.12 IR active mode of frequency 455 cm^{-1}

Figure 3.9.12 gives the most prominent of the IR active modes for this structure which is 455 cm^{-1} . This looks like a mixture of stretching and bending vibration mode. As can be seen from the Table 3.10.1 the permanent dipole moments of the clusters other than the dimer is vanishingly small. However, the vibrational motion can result in a large change of dipole moments which results in peaks in IR spectrum.

In the Raman Spectra (Figure 3.9.13) of Zn_4S_4 we can see about 5 active modes, the most prominent being at 60 cm^{-1} and another one at 330 cm^{-1} . The frequencies 95 cm^{-1} and 120

cm^{-1} look like the condition of Fermi Resonance. We also see some very soft modes for this structure. However these modes are not IR or Raman active. The presence of soft modes indicates that the cluster is likely to change its structure at elevated temperature.

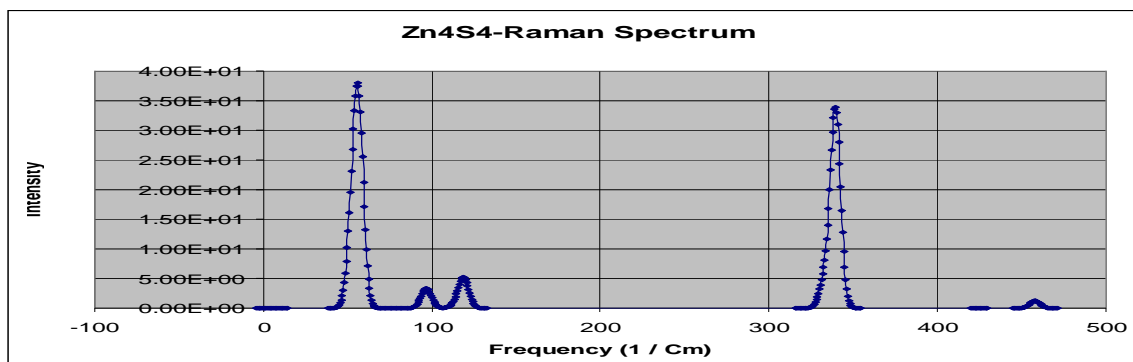


Figure 3.9.13 Raman Spectrum of Zn_4S_4

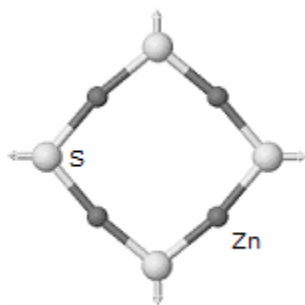


Figure 3.9.14 Raman mode of Frequency 330 cm^{-1}

Figure 3.9.14 shows the breathing mode of Raman Spectra of highest intensity and of frequency 330 cm^{-1} .

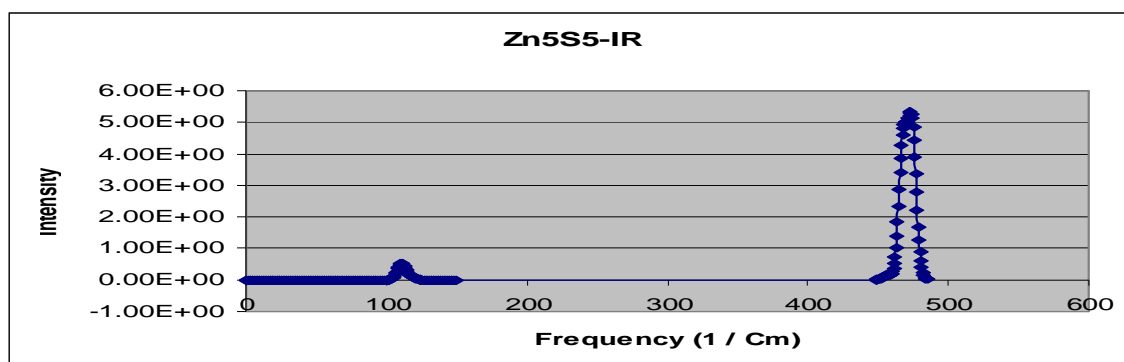


Figure 3.9.15 IR Spectrum of Zn_5S_5

The IR Spectrum of Zn_5S_5 is shown in Figure 3.9.15. Out of the 24 vibrational modes only 2 modes are IR active with substantial intensity. The lower intensity peak occurs at 110 cm^{-1} and the higher intensity at 475 cm^{-1} . This is a nearly pentagonal structure and the only mode inducing large change in dipole moment is an out of plane bending mode.



Figure 3.10.16 IR active mode with frequency 475 cm^{-1}

Figure 3.9.16 shows the 475 cm^{-1} active mode. From the atoms vibration directions it may be guessed as it is a mixture of deformation and stretching modes.

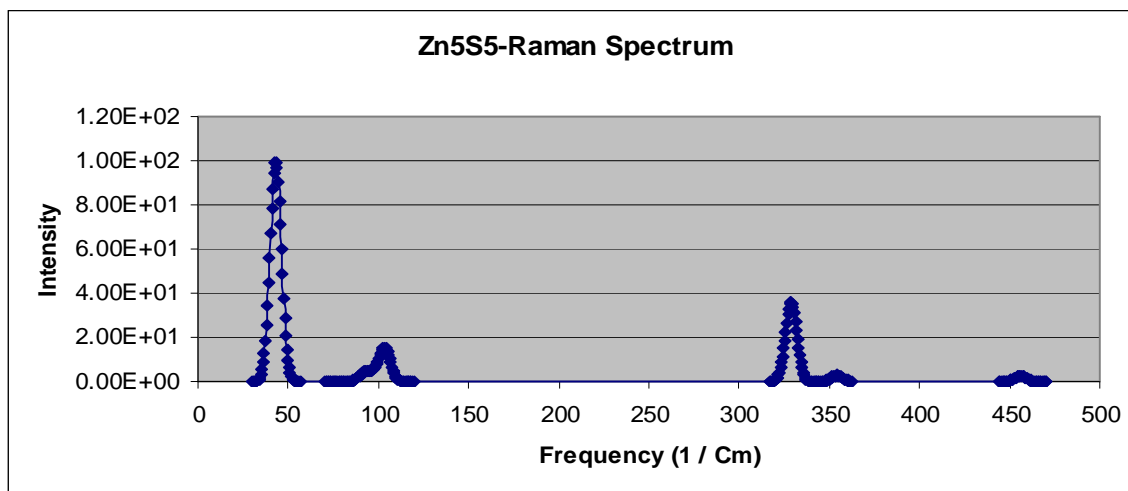


Figure 3.9.17 Raman Spectra of Zn_5S_5

Figure 3.10.17 gives the Raman Spectra of Zn_5S_5 , which shows about 3 peaks with substantial intensities with lowest intensity peak being at 100 cm^{-1} and the highest intensity occurring at 45 cm^{-1} . The presence of soft modes in this cluster also indicates that the cluster will undergo shape change at elevated temperature. The highest intensity mode is shown in Figure 3.9.18 which shows a breathing-like mode involving only the sulfur atoms.

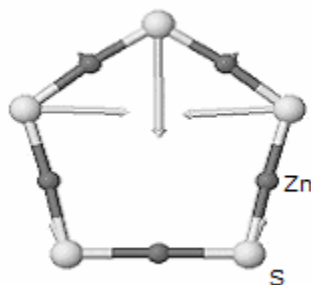


Figure 3.9.18 Raman vibration mode for 45 cm^{-1}

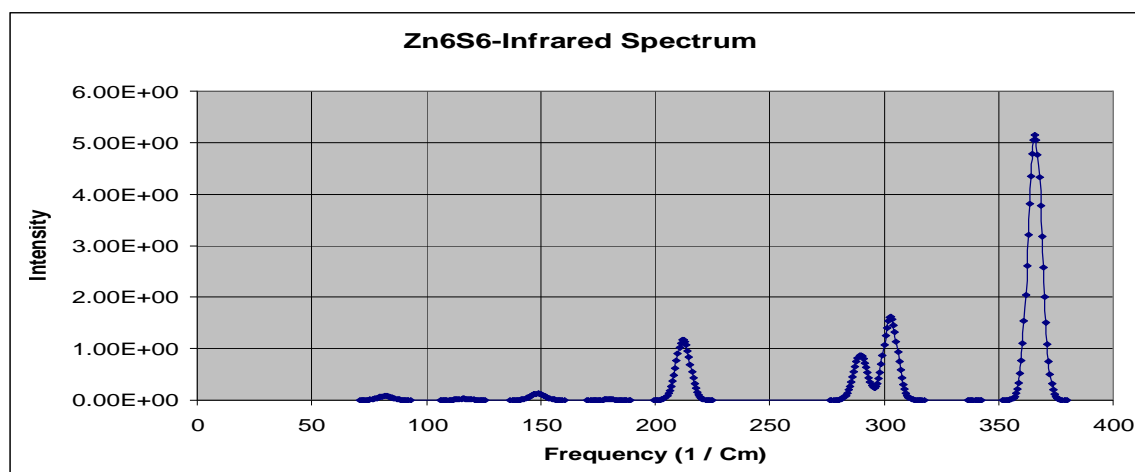


Figure 3.9.19 IR Spectra of Zn_6S_6

The IR spectrum of Zn_6S_6 is shown in Figure 3.9.19. The structure should have 30 vibrational modes. Only 4 modes are found to be IR active modes with substantial peak height. It can be seen that the mode with frequency 366 cm^{-1} has high intensity compared to the other peaks. The other frequencies are 212 cm^{-1} , 289 cm^{-1} and 305 cm^{-1} .

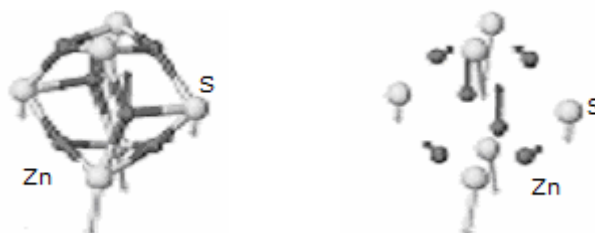


Figure 3.9.20 Highest IR active mode of Zn_6S_6

Vibration mode of IR frequency 366 cm^{-1} is shown in Figure 3.9.20. This mode shows out of phase distortions of the Zn and S atoms. In Figure 3.9.21 Raman Spectra of Zn_6S_6 is shown. About 7 active Raman modes can be seen the lowest intensity occurring at about 280 cm^{-1} and highest intensity occurring at 315 cm^{-1} .

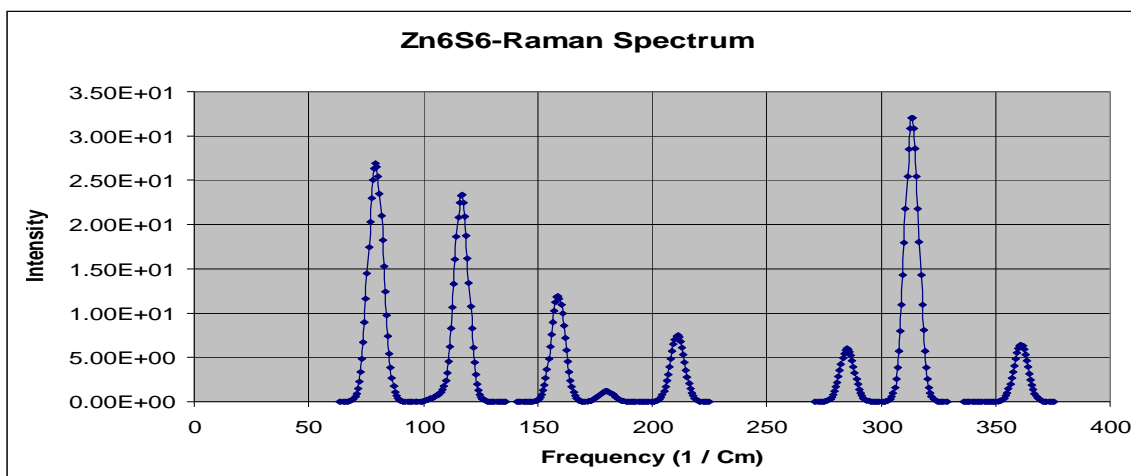


Figure 3.9.21 Raman Spectrum of Zn_6S_6

In Figure 3.9.21 Raman Spectra of Zn_6S_6 is shown. About 7 active Raman modes can be seen the lowest intensity occurring at about 280 cm^{-1} and highest intensity occurring at 315 cm^{-1} . The lowest frequency being at about 70 cm^{-1} and the highest at about 360 cm^{-1} .

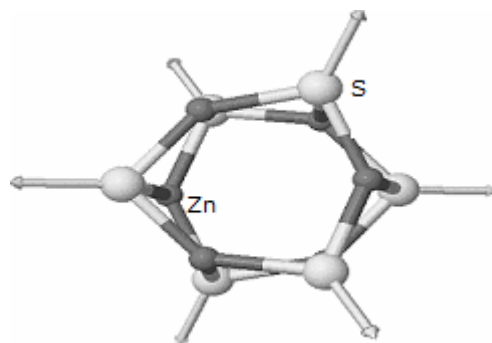


Figure 3.9.22 Breathing mode of highest intensity Raman Spectra

The mode that has highest peak in Raman spectrum is shown in fig. 3.9.22. This is a breathing mode involving the S atoms only. The polarizability of a molecular system scales as its volume. Breathing modes involves significant change in volume and thereby polarizability. Such modes like this therefore show high Raman activity.

3.10 Dipole moment and Polarizability:

Polarizability is an important electronic property that characterizes the system's response to an applied electric field. When a cluster is placed in an applied uniform static (or frequency dependent) electric field, its electronic cloud redistributes in response to the electric field. The polarizability is a measure of the response of electronic distribution to applied electric field. The total energy of the cluster can be expanded as a function of applied electric field using Taylor series. The linear (or dipole) polarizability is the second term in this expansion. It is a tensor of second rank. It is given by

$$\alpha = \begin{pmatrix} \alpha_{xx} & \alpha_{xy} & \alpha_{xz} \\ \alpha_{yx} & \alpha_{yy} & \alpha_{yz} \\ \alpha_{zx} & \alpha_{zy} & \alpha_{zz} \end{pmatrix}, \quad (3.10.1)$$

$$\text{where, } \alpha_{12} = - \left. \frac{\partial^2 E}{\partial F_1 \partial F_2} \right|_{\bar{F}=0}. \quad (3.10.2)$$

The components of the matrix can be obtained from the total energy derivatives with respect to field. A number of methods have been developed to determine the polarizabilities over the years. In this work, we use finite field method in which the perturbation term " $-F.r$ " (both vectors) is added to the Hamiltonian. The field dependent total energies are then obtained by self-consistently solving the Kohn-Sham problem for various field values. Once the total energies are known, the components of polarizability matrix can be obtained using suitable finite difference approximation.

When computing total energy in presence of field one needs to make a suitable choice for the field values. These field values should be large enough to get response but not too large, so that the system's response is in the linear regime. We chose the field values in

step 0.005 atomic units. To obtain full polarizability tensor one needs to perform 13 self-consistent calculations. Very tight self-consistent convergence criteria need to be used to eliminate the numerical noise and obtain accurate response. Thus, the self-consistent solutions for the polarizability are more expensive from self-consistent steps during the structure optimization. The polarizabilities can also be obtained from dipole moments instead of total energies using the same finite-field method. In this work the polarizability is computed from the total energies. The mean polarizabilities are given in Table 3.10.2 along with the permanent dipole moments. Note that other than the ZnS dimer the permanent dipole moment of most clusters is nearly zero. This is due to the fact that most of the clusters have symmetric structure which results in appropriate balance of the positive and negative charge distribution to cancel the overall charge imbalance that would lead to appreciable values of dipole moments. As mentioned earlier, the polarizability is a second order tensor and has six components. The mean polarizability is the one third of trace of the polarizability matrix, that is

$$\alpha_{\text{mean}} = \frac{1}{3} (\alpha_{xx} + \alpha_{yy} + \alpha_{zz}).$$

The polarizability systematically increases with increase in size of cluster. From the classical electronic we know that for a metallic or dielectric sphere the polarizability is roughly proportional to cube of sphere radius. This is related to volume of the systems. As the larger clusters have larger volume, their polarizability is also large. Note however that the polarizability per ZnS pair does not change very rapidly. Below given is the data on Dipole moment, polarizability and mean polarizability of ZnS clusters.

Table 3.10.1 Dipole Moment and its components for ZnS Clusters

Cluster	D_x in Debye	D_y in Debye	D_z in Debye	$D=(D_x^2+ D_y^2+ D_z^2)^{1/2}$ in Debye
Zn ₁ S ₁	-0.00019	-0.00019	-5.025	5.03
Zn ₂ S ₂	0.00007	0.00046	0.015	0.015
Zn ₃ S ₃	0.018	-0.0214	-0.000202	0.027
Zn ₄ S ₄	-0.00218	-0.00087	-0.0021	0.0032
Zn ₅ S ₅	-0.0085	0.022	-0.0023	0.0236
Zn ₆ S ₆	-0.000598	0.0023	-0.002	0.0031

Table 3.10.2 Polarizabilities of ZnS clusters.

Cluster	α_{xx}	α_{yy}	α_{zz}	$(\alpha_{xx}+ \alpha_{yy}+ \alpha_{zz})/3$
Zn ₁ S ₁	7.65	7.65	11.79	9.02
Zn ₂ S ₂	10.78	15.32	17.97	14.69
Zn ₃ S ₃	23.86	23.90	14.20	20.65
Zn ₄ S ₄	32.79	32.79	18.36	27.98
Zn ₅ S ₅	42.16	43.47	22.82	36.15
Zn ₆ S ₆	39.26	39.19	35.56	38.00

SUMMARY

We have studied the structural, electronic, vibrational and optical properties of small stoichiometric clusters $(\text{ZnS})_n$ up to the size $n=6$. We find that the ZnS clusters favor ring-like closed structures up to size $n=5$. Zn_6S_6 cluster favors a three-dimensional structure. This feature is seen in other II-VI semiconductor clusters though the onset of 3D structure varies in different clusters. The structures are closed and have vanishingly small dipole moments. The ZnS dimer has a dipole moment of 5.03 Debye. Our analysis shows that in the ZnS molecule the charge transfer is about 0.8×10^{-19} C. We have also noted that the ZnS dimer has binding energy lower than its first ionization potential which indicates low intensity for this cluster in experiments using cationic clusters. We have calculated the vertical and adiabatic IP and EA for the lowest energy cluster for each size. The calculated adiabatic IP for the clusters studied here ranges from 8.0 to 8.7 eV, the EA ranges from 1.2 – 2.2 eV and the adiabatic EA ranges from 2.2 – 2.02 eV. Only the dimer has an EA above 2 eV which also indicates that it will be more reactive. The HOMO-LUMO gaps of the clusters are presented along with the predictions of the possible utilization of the clusters in photovoltaics and as photocatalysts. Except for the dimer, the larger clusters have gaps ranging from 1.1 to 3 eV. Since DFT is contaminated by self-interaction and as a result produce HOMO-LUMO or band gaps which are in general smaller by 30 -40%, we have adjusted our calculated gaps by this amount. The larger gaps are in good agreement with available experimental values.

All the isomers presented here are vibrationally stable though a few of them have several soft vibrational modes. Presence of soft modes indicates that there will be structural distortions at finite temperature. All our calculations were performed at

temperature $T=0\text{K}$. We have calculated the IR and Raman spectrum of the lowest energy isomer for each size which will help in experimental characterization of these clusters. This is the first time that Raman and IR spectra of these clusters are presented.

APPENDIX

Definitions

Bond Angle: A bond angle is the angle formed between three atoms across at least two bonds.

Bond length: The bond length is defined to be the average distance between the centers of two atoms bonded together in any given molecule.

Binding Energy of a molecule: The energy required to separate atoms from a molecule.

Total Electronic Energy :

$$E = \sum_{\mu\nu} P_{\mu\nu} \left\langle \phi_{\mu} \left| -\frac{\nabla^2}{2} + v_{ext}(\vec{r}) \right| \phi_{\mu} \right\rangle + \frac{1}{2} \sum_{\mu\nu\kappa\lambda} P_{\mu\nu} P_{\kappa\lambda} \iint d\vec{r}_1 d\vec{r}_2 \phi_{\mu} \phi_{\nu} r_{12}^{-1} \phi_{\kappa} \phi_{\lambda} + E_{xc}[\rho(\vec{r})] \quad (\text{A.1})$$

Vertical Ionization Potential: It is the energy required to remove an electron instantaneously completely from a gaseous atom, molecule or ion.

$$\text{I.P.}_{\text{instantaneous}} = E_{\text{instantaneous}}[n-1] - E_{\text{relaxed}}[n], \quad (\text{A.2})$$

where ‘n’ is the number of electrons present in the atom or molecule or ion.

Adiabatic Ionization Potential [30]: It is the energy required to remove an electron from the molecule in its ground vibrational and rotational state to produce a molecular ion in its ground vibrational and rotational state.

$$\text{I.P.}_{\text{relaxed}} = E_{\text{relaxed}}[n-1] - E_{\text{relaxed}}[n] \quad (\text{A.3})$$

Vertical Electron Affinity [30]: The electron affinity E_a of an atom or molecule is the energy released in the process of adding an electron instantaneously.

$$E_{a \text{ inst}} = E_{a \text{ relaxed}}[n] - E_{a \text{ instantaneous}}[n+1] \quad (\text{A.4})$$

Adiabatic Electron Affinity: The energy released when an electron is added to an atom or molecule and is allowed to relax.

$$E_{a \text{ relaxed}} = E_{\text{relaxed}}[n] - E_{\text{instantaneous}}[n+1] \quad (\text{A.5})$$

REFERENCES

1. Transmission electron microscopy of CdTe/CdS based solar cells Y. Y. Loginov, K. Durose, H. M. Al-Allak, S. A. Galloway, S. Oktik, A. W. Brinkman, H. Richter, and D. Bonnet, *J. Cryst. Growth* 161, 159 (1996).
2. Effects of the Au/CdTe back contact on IV and CV characteristics of Au/CdTe/CdS/TCO solar cells A. Niemegeers and M. Burgelman, *J. Appl. Phys.* 81, 2881 (1997).
3. A microstructural study on the surface and interface of CdTe/CdS solar cells K. Li, A. T. S. Wee, J. Lin, K. L. Tan, L. Zhou, S. F. Y. Li, Z. C. Feng, H. C. Chou, S. Kamra, and A. Rohatgi, *J. Mater. Sci.: Mater. Electron.* 8, 125 (1997).
4. Approach toward high efficiency CdTe/CdS heterojunction solar cells H. C. Chou, A. Rohatgi, N. M. Jokerst, S. Kamra, S. R. Stock, S. L. Lowrie, R. K. Ahrenkiel, and D. H. Levi, *Mater. Chem. Phys.* 43, 178 (1996).
5. Q-sized cadmium sulfide: synthesis, characterization, and efficiency of photoinitiation of polymerization of several vinylic W A. J. Hoffman, G. Mills, H. Yee, and M. R. Hoffmann, *J. Phys. Chem.* 96, 5546 (1992).
6. A photodetector based on ZnCdS nanoparticles in a CdS matrix formed by screen printing and sintering of CdS and ZnC12 P. J. Sebastian and M. Ocampo, *Sol. Energy Mater. Sol. Cells* 44, 1 (1996).
7. *Sprintronic: Fundamentals and applications*, Zutic, I., Dabian, J., and Das Sarma, S., *Rev. Modern Phys.*, 76, (2), pp. 323–410, 2004.
8. Electronic excitation energies of Zn*i*Si clusters Jon M. Matxain, Arantxa Irigoras, Joseph E. Fowler, and Jesus M. Ugalde *Phys. Rev. A*, 64, 013201 (2001).
9. Electronic excitation energies of small Zn*i*Si clusters Jon M. Matxain, Arantxa Irigoras, Joseph E. Fowler, and Jesus M. Ugalde *Phys. Rev. A* 63, 013202 (2000).
10. Small Clusters of II-VI materials: Zn_{*i*}Si, *i* = 1-9 Jon M. Matxain, Arantxa Irigoras, Joseph E. Fowler, and Jesus M. Ugalde *Phys. Rev. A* 61, 053201 (2000)
11. Clusters of II-VI Materials: Cd_{*i*}X_{*i*}, X = S, Se, Te, *i* ≤ 16 Jon M. Matxain, Jose M. Mercero Joseph E. Fowler, and Jesus M. Ugalde *Phys. Rev. A* 108, 10502 (2004).
12. Clusters of Group II-VI Materials: Cd_{*i*}O_{*i*} (*i* ≤ 15) Jon M. Matxain, Jose M.

Mercero Joseph E. Fowler and Jesus M. Ugalde J. Phys. Chem A 107, 9918 (2003).

13. Photophysical properties of ZnS quantum dots Li YD, Ding Y, Zhang Y, Qian J. Physics and Chemistry of Solids 60 (1999) 13-15.
14. Pseudopotential Plane wave calculations for ZnS J. L. Martins and N. Troullier, Phys. Rev. B 43, 2213 (1991).
15. Electronic, Optical, and structural properties of some wurtzite crystals Y. N. Xu and W. Y. Ching, Phys. Rev. B 48, 4335 (1993).
16. Cage and tube structures of medium-sized zinc oxide clusters (ZnO)_n (n= 24, 28, 36, and 48), B.Wang, X. Wang, G. Chen, S.Nagase, J. Zhao, J. Chem. Phys. 128, 144710 (2008).
17. ZnS bubble clusters with Onion-like structures, Eleonora Spano, Said Hamad and C. Richard A. Catlow, Chem. Comm. 864-865, 2004.
18. Ab initio models for ZnS surfaces: J. Muilu and T. A. Pakkanen, Phys. Rev. B 49, 11 185 (1994).
19. First-Principles calculation of the electronic structure of the wurtzite semiconductors ZnO and ZnS P. Schroer, P. Kruger, and J. Pollmann, Phys. Rev. B 47, 6971 (1993).
20. Self-interaction and relaxation-corrected pseudopotentials for II-VI semiconductors D. Vogel, P. Kruger, and J. Pollmann, Phys. Rev. B 54, 5495 (1996).
21. Small, Nonstoichiometric Zinc Sulfide Clusters Krum Chuchev and Joseph J. BelBruno, J. Phys. Chem. A 2005, 109, 1564-1569.
22. Size-dependent Properties of Zn_mS_n clusters: A density-functional tight-binding study Pal, Goswami and Sarkar J. Chem Phys. 123, 044311 (2005).
23. Quantum Crystalites and Non-linear Optics, L. Brus, Applied Phys. A 53, 465-474 (1991).
24. Ab-initio calculations of small Cd_xS_y and Zn_xS_y (x,y ≤ 6) clusters, Gurin, V.S. , Solid State Communications, 108 (6), p.389-392, Oct 1998.
25. The Nature of the Chemical Bond and the Structure of Molecules and Crystals, LINUS PAULING, 3rd edition.
26. Introduction to Solid State Physics, CHARLES KITTEL, 8th edition.

27. Bonding Energy levels & Bands in Inorganic Solids, J.A.DUFFY, 1990.
28. Web site of The Technical Glass Company. Glass and Ceramics for Science and Industry.
29. A Chemist's Guide to Density Functional Theory. W. Koch and M. C. Holthausen. Wiley-VCH Verlag GmbH, Weinheim (2000).
30. Density-Functional Theory of Atoms and Molecules. R. G. Parr and W. Yang. Oxford University Press, Oxford (1989).
31. Density Functional Theory – An Approach to the Quantum Many-Body Problem. R.M. Dreizler and E. K. U. Gross. Springer Verlag, Berlin (1990).
32. Density Functional Methods in Chemistry. J. K. Labanowsky and J. W. Andzelm (Editors). Springer Verlag, New York (1991).
33. Density Functional Theory. In European Summerschool in Quantum Chemistry 2003, Book II, N. C. Handy. Edited by B. O. Roos and P.-O. Widmark, pp. 503-545. Lund University, Lund, 3rd edition (2003).
34. The Fundamentals of Density Functional Theory. H. Eschrig. EAGLE, Leipzig, 2nd Edition (2003).
35. A Primer in Density Functional Theory. Lecture Notes in Physics. C. Fiolhais, F. Nogueira and M. A. L. Marques. Springer Verlag, Berlin (2003).
36. E. J. Baerends and O. V. Gritsenko. A Quantum Chemical View of Density Functional Theory. J. Phys. Chem. A 101, 5383-5403 (1997).
37. The Calculation of Atomic Fields. L. H. Thomas. Proc. Camb. Phil. Soc. 23, 542 (1927).
38. Un Metodo Statistico per la Determinazione di Alcune Propriet'a dell' Atomo. E. Fermi. Rend. Accad. Lincei 6, 602 (1927).
39. A Simplification of the Hartree-Fock Method. J. C. Slater Phys. Rev. 81,385-390 (1951).
40. Note on Exchange Phenomena in the Thomas Atom. P. A. M. Dirac. Proc. Camb. Philos. Soc. 26, 376 (1930).
41. Inhomogeneous Electron Gas. P. Hohenberg and W. Kohn. Phys. Rev. 136, B864-B871 (1964).

42. Electron densities in search of Hamiltonians. M. Levy Phys. Rev. A 26, 1200-1208 (1982).
43. Self-Consistent Equations Including Exchange and Correlation Effects. W. Kohn and L. Sham. Phys. Rev. 140, A1133-A1138 (1965).
44. Ground State of the Electron Gas by a Stochastic Method. D. M. Ceperley and B. J. Alder. Phys. Rev. Lett. 45, 566-569 (1980).
45. Accurate spin-dependent electron liquid correlation energies for local spin density calculations: a critical analysis. S. Vosko, L. Wilk and M. Nusair. Can. J. Phys. 58, 1200 (1980).
46. Self-interaction correction to densityfunctional approximations for many-electron systems. J. P. Perdew and A. Zunger. Phys. Rev. B 23, 5048-5079 (1981).
47. Accurate and simple analytic representation of the electron-gas correlation energy. J. P. Perdew and Y. Wang. Phys. Rev. B 45, 13244-13249 (1992).
48. Density-functional exchange-energy approximation with correct asymptotic behavior. A. D. Becke. Phys. Rev. A 38, 3098-3100 (1988).
49. Accurate and simple density functional for the electronic exchange energy: Generalized gradient approximation. J. P. Perdew and Y. Wang. Phys. Rev. B 33, 8800-8802 (1986).
50. Density-functional approximation for the correlation energy of the inhomogeneous electron gas. J. P. Perdew. Phys. Rev. B 33, 8822-8824 (1986).
51. Correlation energy of an inhomogeneous electron gas: A. D. Becke. A coordinate-space model. J. Chem. Phys. 88, 1053-1062 (1988).
52. Development of the Colle-Salvetti correlation-energy formula into a functional of the electron density. C. Lee, W. Yang and R. G. Parr. Phys. Rev. B 37, 785-789 (1988).
53. Atoms, molecules, solids, and surfaces: Applications of the generalized gradient approximation for exchange and correlation. J. P. Perdew, J. A. Chevary, S. H. Vosko, K. A. Jackson, M. R. Pederson, D. J. Singh and C. Fiolhais. Phys. Rev. B 46, 6671- 6687 (1992). *ibid* 48, 4978 (1993).
54. Generalized gradient approximation for the exchange-correlation hole of a many-electron system. J. P. Perdew, K. Burke and Y. Wang. Phys. Rev. B 54, 16533-16539 (1996).

55. Generalized Gradient Approximation Made Simple. J. P. Perdew, K. Burke and M. Ernzerhof. Phys. Rev. Lett. 77, 3865-3868 (1996). *ibid* 78, 1396 (1997).
56. Variational mesh for quantum-mechanical simulations M. R. Pederson and K. A. Jackson, Phys. Rev. B. 41, 7453 (1990)
57. Optimization of Gaussian basis sets for density-functional calculations .D. V. Porezag and M. R. Pederson, Phys. Rev. A 60, 2840 ~ (1999).
58. Infrared intensities and Raman-scattering activities within density-functional theory D.V. Porezag and M. R. Pederson, Phys. Rev. B 54, 7830 ~(1996).
59. Accurate forces in a local-orbital approach to the local density approximation. K. A. Jackson and M. R. Pederson, Phys. Rev. B. 42, 3276 (1990).
60. Pseudoenergies for simulations on mechanical systems. M. R. Pederson and K. A. Jackson, Phys. Rev. B. 43, 7312 (1991).
61. Vibrational frequencies and intensities of small molecules: All-electron, pseudopotential, and mixed-potential methodologies A. Briley, M. R. Pederson, K. A. Jackson, D. C. Patton, and D. V. Porezag, Phys. Rev. B. 58, 1786 (1998).
62. A. A. Quong, M. R. Pederson, and J. L. Feldman, Solid State Commun. 87, 535 (1993)
63. D. V. Porezag, PhD thesis: <http://archiv.tu-chemnitz.de/pub/1997/0025>.
64. Infrared and Raman Spectroscopy methods and applications, Edited by Bernhard Schrader, VCH, 1995.
65. $Zn_nS_m^+$ cluster production by laser ablation A. Burnin, J. J. BelBruno, Chem Phys Lett, 362, 341 (2002).
66. Cobalt doped rings and cages of ZnO clusters: Motifs for magnetic cluster-assembled materials A.C. Reber, S.N. Khanna, J.S. Hunjan, M.R. Beltrán, Chem Phys Lett, 428, 376(2006).
67. Computational study of the relative stabilities of ZnS clusters, for sizes between 1 and 4 nm, Said Hamad, C. Richard A. Catlow, J. Cryst. Growth, 2-8, 294 (2006).
68. A theoretical study on size-dependent properties of rock-salt ZnS clusters, Sougata Pal, Biplab Goswami and Pranab Sarkar, Computing Letters, 1, no 4, 297-303 (2005)
69. <http://rredc.nrel.gov/solar/spectra/am1.5/>

CURRICULUM VITAE

Venkata Ramana Chaganti, the second child of Sunder Rao Chaganti and Rajyalaxmi Chaganti, was born in Vishakapatnam, Andhra Pradesh, India. He did his bachelor's in Biomedical Engineering from Osmania University in 1988. He then worked with Micronic Devices, India as sales and service engineer for about a year. He then joined as a lecturer to teach Mathematics and Physics for High School students. After working for about 9 years he joined Advanced technology Labs, Chennai, India as a software Trainee. After two years he rejoined the teaching community to continue as lecturer at various capacities at various institutions. He moved to United States of America in July, 2007. In pursuit of knowledge he joined as a graduated student at University of Texas at El Paso in spring 2008. During his M.S. he worked with Dr. Tunna Baruah as a research assistant.

Permanent Address: 4234 Canyon Glen Circle,

Austin, Texas – 78732

This thesis was typed by Venkata R. Chaganti.